

Atmospheric Turbulence Modeling and Aperture Analysis
for Optimizing Receiver Design and System Performance
on Free Space Optical Communication Links

A THESIS

SUBMITTED TO THE DEPARTMENT OF ELECTRICAL AND
ELECTRONICS ENGINEERING

AND THE GRADUATE SCHOOL OF ENGINEERING AND SCIENCES
OF BILKENT UNIVERSITY

IN PARTIAL FULFILLMENT OF THE REQUIREMENTS

FOR THE DEGREE OF
MASTER OF SCIENCE

By

Hasim Meric

September 2012

I certify that I have read this thesis and that in my opinion it is fully adequate,
in scope and in quality, as a thesis for the degree of Master of Science.

Prof. Dr. Ayhan Altıntaş(Supervisor)

I certify that I have read this thesis and that in my opinion it is fully adequate,
in scope and in quality, as a thesis for the degree of Master of Science.

Assist. Prof. Dr. Heba Yüksel(Co-supervisor)

I certify that I have read this thesis and that in my opinion it is fully adequate,
in scope and in quality, as a thesis for the degree of Master of Science.

Assoc. Prof. Dr. Vakur B. Ertürk

I certify that I have read this thesis and that in my opinion it is fully adequate,
in scope and in quality, as a thesis for the degree of Master of Science.

Assist. Prof. Dr. Ömer İlday

Approved for the Graduate School of Engineering and Sciences:

Prof. Dr. Levent Onural
Director of Graduate School of Engineering and Sciences

ABSTRACT

Atmospheric Turbulence Modeling and Aperture Analysis for Optimizing Receiver Design and System Performance on Free Space Optical Communication Links

Hasim Meric

M.S. in Electrical and Electronics Engineering

Supervisor: Prof. Dr. Ayhan Altıntaş
and Assist. Prof. Dr. Heba Yüksel

September 2012

Strong turbulence measurements that are taken using real time optical wireless experimental setups are valuable when studying the effects of turbulence regimes on a propagating optical beam. In any kind of Free Space Optical (FSO) system, knowing the strength of the turbulence thus the refractive index structure constant (C_n^2), is beneficial for having an optimum bandwidth of communication. Even if the FSO Link is placed very well-high-above the ground just to have weak enough turbulence effects, there can be severe atmospheric conditions that can change the turbulence regime. Having a successful theory that will cover all regimes will give us the chance of directly processing the image in existing or using an additional hardware thus deciding on the optimum bandwidth of the communication line at firsthand. In literature, simulation of beam propagation through turbulent media has always been a tricky subject when it comes to moderate-to-strong turbulent regimes. Creating a well controlled turbulent environment is beneficial as a fast and a practical approach when it comes to testing the optical wireless communication systems in diverse atmospheric conditions.

For all of these purposes, strong turbulence data have been collected using an outdoor optical wireless setup placed about 85 centimeters above the ground with an acceptable declination and a path length of about 250 meters inducing strong turbulence to the propagating beam. Variety of turbulence strength estimation methods as well as frame image analysis techniques are then been applied to the experimental data in order to study the effects of different parameters on the result. Such strong turbulence data is compared with existing weak and intermediate turbulence data. The Aperture Averaging (AA) Factor for different turbulence regimes as well as the inner and outer scales of atmospheric turbulence are also investigated. A new method for calculating the Aperture Averaging Factor is demonstrated deducing spatial features at the receiver plane. Controlled turbulent media is created using multiple phase screens each having supervised random variations in its frequency and power while the propagated beam is calculated using Fresnel diffraction method. The effect of the turbulent media is added to the propagated beam using the modified Von Karman spectrum. Created scintillation screens are tested and compared with the experimental data which are gathered in different turbulence regimes within various atmospheric conditions. We believe that the general drawback of the beam propagation simulation is the difference in terms of spatial distribution and sequential phase textures. To overcome these two challenges we calculate the Aperture Averaging Factors to create more realistic results. In this manner, it is possible to create more viable turbulent like scintillations thus the relationship between the turbulence strength and the simulated turbulence parameters are distinctly available. Our simulation gives us an elusive insight on the real atmospheric turbulent media. It improves our understanding on parameters that are involved in real time intensity fluctuations that occur in every optical wireless communication system.

Keywords: Free Space Optical Communication (FSO), Optical Wireless Links, Refractive Index Structure Constant(C_n^2), Intensity Variance, Rytov Variance,

Strong Atmospheric Turbulence, Scintillation Index, Aperture Averaging, Point Averaged Aperture Averaging, Phase Screens.

ÖZET

AÇIK ALAN OPTİK KOMÜNİKASYON LİNKLERİ SİSTEM PERFORMANSI İÇİN ATMOSFERİK TÜRBÜLANS MODELLEME VE OPTİMUM ALICI AÇIKLIK ANALİZİ

Hasim Meric

Elektrik ve Elektronik Mühendisliği Bölümü Yüksek Lisans

Tez Yöneticisi: Prof. Dr. Ayhan Altıntaş

ve Prof. Assist. Prof. Dr. Heba Yüksel

Eylül 2012

Gerçek zamanlı optik telekomünikasyon linkleri kullanılarak alınan güçlü türbülans Ölçümleri atmosferde ilerleyen Işık huzmesi üzerindeki atmosferik etkileri incelemek için çok değerlidir. Kullanılan herhangi bir açık alan optik komünikasyon linkinde kırılma indisi yapısal sabitini bilmek veya kestirmek iletişim hattının optimum bant genişliği hakkında bilgi edinmek için pek değerlidir. Açık alan komünikasyon linkinin çok yüksek noktalara konuşlandırıldığı durumlarda bile iki alışverişçi arasında beklenmedik türbülans etkileri görülebilmektedir. Tüm türbülans rejimlerini kapsayacak genel bir teoremin varlığı alıcı tarafında eşzamanlı sinyal işleyerek veya ek bir donanım yardımı ile komünikasyon linkinin optimum bant genişliğini ilk elde belirlemede etkili olacaktır. Literatürde ışık huzmesinin türbülans ortamında ilerlemesi özellikle orta ve yüksek güçteki türbülans medyaları için dikkat çekici bir konu olmuştur. İyi kontrol edilmiş ve belirlenen güçte türbülans etkimiş bir ışık huzmesi simülasyonu yapmak açık alan optik komünikasyon linkleri için hızlı pratik ve işe yarar bir yöntem teşkil etmektedir.

Tüm bu nedenlerden dolayı, güçlü türbülans verisi yerden 85 cm yükseklik ve de kabul edilebilir eğimi olan 250 m uzunlukta deneysel bir alanda kurulan açık alan optik iletişim kurulumundan yararlanılarak elde edilmiştir. Türbülansa etkiyen ve tetikleyen parametreler hakkında bilgi sahibi olabilmek için çeşitli türbülans güç hesaplama ve kestirim metotlarının yanında eşzamanlı çerçeve görüntü analiz metotları da geliştirilmiştir. Elde edilen veriler var olan zayıf ve orta güçteki türbülans verileri ile karşılaştırılmıştır. Farklı güçteki türbülans verilerinin ortalama açıklık faktörünün yanında atmosferik güç spektrumunun içsel ve dışsal skala değerleri araştırılmıştır. Ortalama açıklık faktörü hesaplanmak üzere mekansal özellikleri kullanarak yeni bir metot sunulmuştur. Gücü kontrol edilebilir bir türbülans ortamı seri olarak önceden ortalaması ve de varyansı karar verilmiş rastgele atanmış frekans ve güç değerlerine sahip faz ekranları kullanılıp ışık huzmesinin yayılımı açısız frensel kırılım metodu kullanılarak oluşturulmuştur. Türbülans ortamının etkisi modifiye edilmiş von Karman spektrumu kullanılarak yayılan ışık huzmesine etkimıştır. Alıcıda Yaratılan ışıltama faz ekranı ile farklı türbülans rejimlerinde ve farklı deney ortamlarında alınan deneysel verilerimizin sonuçları karşılaştırılıp test edilmiştir. Kestirilmektedir ki literatürdeki atmosferik ışık huzmesi yayılımındaki sonuçlara engel teşkil eden faktörler sıralı atmosferik faz dokusu ve de yüzeysele dağılımıdır ışık huzmesi dağılımıdır. Bu iki engelin üstesinden gelebilmek için simülasyon ve deneysel sonuçların ortalama açıklık faktörleri hesaplanmıştır. Bu sayede gerçeğe daha yakın türbülans ışıltamaları elde etmek mümkün olup farklı türbülans rejimlerinde türbülansa etki eden parametreler belirgin hale gelmektedir. Simülasyon sonuçlarımız bize türbülans doğası ve ortamı hakkında ele gelmez bir içgörü vermektedir. Aynı zamanda gerçek zamanlı tüm optik açık alan iletişim linklerinde temel problem olan güç yoğunluğu dalgalanmaları üzerinde etkili olan parametreler üzerindeki anlayışımızı güçlendirmektedir.

Anahtar Kelimeler: Açık Alan Optik İletim, Kablosuz Optik Linkleri, Kırılma indisi kalıpsal sabiti, Güç Yoğunluğu Varyansı, Rytov Varyansı, Güçlü

Atmospheric Turbulence, Işıldama İndisi, Açıklık Ortalaması, Nokta Ortalamalı
Açıklık Ortalama, Faz Ekranı

ACKNOWLEDGMENTS

First of all, I would like to give my inexpressible gratitude to my main supervisor Assist. Prof. Heba Yüksel, who was the most inspiring and influential person during my graduate studies. She has provided me with a great research environment with her positiveness, friendly approach and endless support. It was a great honor and privilege for me to work with her. My deepest respects and thanks goes to Prof. Ayhan Altıntaş for agreeing to serve as my supervisor at the end of my thesis work.

Also, I would like to thank Assoc. Prof. Vakur Ertürk and Asst. Prof. Ömer İlday for their service in my thesis committee.

Finally, I especially would like to thank my family for their unconditional love and support.

Contents

1	INTRODUCTION	1
1.1	Overview of Turbulence	1
1.2	Classical Theory	4
1.3	Aperture Averaging Theory	7
2	Simulation Model	10
2.1	Refractive Index Structure Constant (C_n^2) Evaluation	10
2.2	Phase Screen Method	14
2.2.1	Introduction	14
2.2.2	Phase screen Methodology	16
2.2.3	Results	20
2.3	Image Acquisition and Tracking Algorithm	24
2.4	Analysis of turbulence strength for free space optical communica- tion using Support Vector Machine (SVM) regression methods . .	28
2.4.1	Introduction	28

2.4.2	Feature Extraction	29
2.4.3	Region Covariance Method	29
2.4.4	Discrete wavelet transform (DWT)	30
2.4.5	Complex Wavelet Transform	31
2.4.6	Support Vector Machine Classification	31
2.4.7	SVM Regression	32
2.4.8	Results and Conclusions	41
3	Experimental Setup	42
3.1	Strong Turbulence Setup	42
3.1.1	Odeon Experimental Setup at Bilkent University	42
3.1.2	Strong Turbulence Experiment at the University of Maryland	49
3.2	Acquiring further weak & intermediate turbulence data using the University of Maryland Setup	58
3.3	Analysis of the turbulence results in weak-to-strong turbulence regimes	61
3.4	Proposed Methods for Estimating C_n^2 :	64
3.4.1	Portable C_n^2 Measurement using an Incoherent Source: . .	64
3.4.2	Turbulence Strength Estimation with Tracking Algorithm of the Beam from the Angle of Arrival (AOA) Variance . .	66
4	Model of Turbulence in all of the Turbulence Regimes	69

4.1	Comparison of the strong turbulence data with theory	69
4.2	The Andrews Asymptotic Analysis	70
4.3	Churnside's Asymptotic Analysis	71
4.4	Effective Kolmogorov Spectrum and Scintillation Index	72
4.5	Comparison of the experimental data to the theory	74
4.6	Effects of the inner scale	79
4.7	Optimizing Receiver Design through analysis of the Aperture Averaging curves	81
4.8	Optimizing System Performance through SNR and BER analysis	82
5	Conclusion	91

List of Figures

1.1	Atmospheric Layers. Source: <i>Larry C. Andrews,Laser Beam Propagation Through Random Media,pg:10</i>	2
1.2	Typical atmospheric transmittance for 1 km horizontal path, 3 meters above the ground, no fog, no rain, no clouds. Source: <i>Larry C. Andrews,Laser Beam Propagation Through Random Media,pg:13</i>	4
1.3	The Cascade theory of turbulence where L_o denotes the outer scale and l_o is the inner scale. Source: <i>Larry C. Andrews,Laser Beam Propagation Through Random Media,pg:60</i>	5
2.1	The C_n^2 image where the refractive index fluctuations occurs . . .	13
2.2	Modified Von Karman Spectrum vs the Von Karman spectrum . .	16
2.3	Fast Fluctuation Effect of the Optical turbulence on a 100 meter slant path with a $C_n^2 = 10^{-16}$	18
2.4	Lower Fluctuation Effect of the Optical turbulence on a 100 meter slant path with a $C_n^2 = 10^{-16}$	19
2.5	Simulation Result of Optical turbulence screen on a 100 meter slant path with a $C_n^2 = 10^{-16}$	20

2.6	Strong Turb. ($C_n^2 = 10^{-10}$) and Intermediate Turb. ($C_n^2 = 10^{-13}$) Images, Path:100 m. $l_0 = 5mm$ and $L_0 = 10^4$	21
2.7	Weak Turb. Image, Path:100 m. $C_n^2 = 10^{-15}$, $l_0 = 5mm$ and $L_0 = 10^4$	21
2.8	Simulated Aperture Averaging Results over 100 meters for various C_n^2 values	22
2.9	Experimental and Simulated Results of the Point Averaged Aper- ture Averaging Factor for $C_n^2 = 2 \times 10^{-12}$, path length =120 meters, $l_0 = 5mm$ and $L_0 = 10^4$	23
2.10	Experimental and Simulated Results of the Point Averaged Aper- ture Averaging Factor for $C_n^2 = 5 \times 10^{-14}$, path length =120 meters, $l_0 = 5mm$ and $L_0 = 10^4$	23
2.11	Intensity Distribution of the Image at the Receiver Side with no Turbulence Effects.	24
2.12	The view of the light path in the optical design of the telescope .	24
2.13	Turbulence induced image and Region result of the software . . .	25
2.14	Turbulence induced problematic image and the Region that is causing problems	26
2.15	Binary image without smoothing and Binary image after smoothing	26
2.16	SVM Regression using 1-Level Wavelet transform with biorthogonal filter	33
2.17	SVM Regression using 1-Level Wavelet transform with biorthogonal filter	33

2.18 SVM Regression using 3-Level Wavelet transform with biorthogonal filter	34
2.19 SVM Regression using 3-Level Wavelet transform with biorthogonal filter	34
2.20 SVM Regression using 1-Level Wavelet transform with doubechies filter	35
2.21 SVM Regression using 1-Level Wavelet transform with doubechies filter	35
2.22 SVM Regression using 3-Level Wavelet transform with doubechies filter	36
2.23 SVM Regression using 3-Level Wavelet transform with doubechies filter	36
2.24 SVM Regression using Region Covariance method with first order statistics	36
2.25 SVM Regression using Region Covariance method with first order statistics	37
2.26 SVM Regression using Region Covariance method with second order statistics	37
2.27 SVM Regression using Region Covariance method with second order statistics	37
2.28 SVM Regression using 1-Level Complex Wavelet transform . . .	38
2.29 SVM Regression using 1-Level Complex Wavelet transform . . .	38
2.30 SVM Regression using 2-Level Complex Wavelet transform . . .	38

2.31	SVM Regression using 2-Level Complex Wavelet transform . . .	39
2.32	SVM Regression using 3-Level Complex Wavelet transform . . .	39
2.33	SVM Regression using 3-Level Complex Wavelet transform . . .	40
2.34	SVM Regression using 4-Level Complex Wavelet transform . . .	40
2.35	SVM Regression using 4-Level Complex Wavelet transform . . .	40
3.1	Aperture Averaging Factor For Intermediate turbulence conditions	43
3.2	Experimental Location	44
3.3	Enclosed Transmitter and Transmitter part front-view	45
3.4	Transmitter side with line-of-sight and Transmitter side (close view)	45
3.5	Receiver part - Front view and Receiver Part - Back view	46
3.6	The receiver side showing line of sight. and Receiver side connected to CCD camera with an adapter	47
3.7	Sample images from Bilkent University Strong Turbulence Setup.	47
3.8	AA factor for the Bilkent University Strong Turbulence Setup. . .	48
3.9	Overall Schematic of the experiment.	49
3.10	Line of Sight shown from the TX side.	50
3.11	Top view of the experiment.	50
3.12	Transmitter Side.	51
3.13	Receiver Side.	52
3.14	Faulty images with high gain settings.	53

3.15 Histogram of Faulty images.	53
3.16 Histogram of Appropriate images.	54
3.17 Sample of a strong turbulence induced beam shape	54
3.18 Aperture averaging factor for different center points on the beam.	55
3.19 Point Averaged Aperture Averaging Factor for strong turbulence data.	55
3.20 Illustration for Point Averaged Aperture Averaging	56
3.21 Point Averaged Aperture Averaging Factor for strong turbulence data.	57
3.22 Weak-Intermediate Turbulence FSO Link.	58
3.23 Weak Turbulence Beam Shape Results.	59
3.24 Aperture Averaging Factor For weak turbulence data.	60
3.25 Combined Aperture Averaging Factors for different turbulence regimes.	61
3.26 Combined AA Curves for different turbulence regimes.	62
3.27 Bilkent University Strong Turbulence setup versus UMD Strong Turbulence Setup.	63
3.28 Portable C_n^2 Measurement Setup.	64
3.29 C_n^2 value in 100 meters- Hallway experiment with hotwave plate.	65
3.30 Overall picture of the transmitter with the beam to track on the middle.	68

3.31	Result of the Beam tracking Algorithm.	68
4.1	Experimental Results and Theoretical Results of Aperture Averaging Factor for Cn^2 structure parameter of 2.31×10^{-15} and Resulted Error margin of 36%.	75
4.2	Experimental Results and Theoretical Results of Aperture Averaging Factor for Cn^2 structure parameter of 1.77×10^{-14} and Resulted Error margin of 32%.	75
4.3	Experimental Results and Theoretical Results of Aperture Averaging Factor for Cn^2 structure parameter of 1.73×10^{-14} and Resulted Error margin of 44.76%.	76
4.4	Experimental Results and Theoretical Results of Aperture Averaging Factor for Cn^2 structure parameter of 1.98×10^{-14} and Resulted Error margin of 27.5%.	76
4.5	Experimental Results and Theoretical Results of Aperture Averaging Factor for Cn^2 structure parameter of 1.13×10^{-14} and Resulted Error margin of 50.69%.	77
4.6	Experimental Results and Theoretical Results of Aperture Averaging Factor for Cn^2 structure parameter of 3.24×10^{-14} and Resulted Error margin of 22.97%.	77
4.7	Experimental Results and Theoretical Results of Aperture Averaging Factor for Cn^2 structure parameter of 9.62×10^{-14} and Resulted Error margin of 50.69%.	78
4.8	Experimental Results and Theoretical Results of Aperture Averaging Factor for Cn^2 structure parameter of 1.19×10^{-14} , link length of 951 m, and Resulted Error margin of 12.72%.	78

4.9	Error Margin for 5 cm diameter receiver vs. the C_n^2 structure parameter.	79
4.10	Intensity Variance vs. Rytov Variance for varying inner scale factors.	80
4.11	Intensity Variance vs. Rytov Variance for varying receiving aperture sizes.	81
4.12	3 sec. segments and C_n^2 behavior in time.	84
4.13	Aperture Averaging Factor vs Receiver diameter for 1 seconds of sequential segments for strong turbulence measurements.	86
4.14	SNR rate for strong turbulence measurements in UMD setup for different Aperture diameters at the receiver where $C_n^2 = 6.57 \times 10^{-15}$.	87
4.15	BER rate for strong turbulence measurements in UMD setup for different Aperture diameters at the receiver where $C_n^2 = 6.57 \times 10^{-15}$	87
4.16	SNR rate for strong turbulence measurements in UMD setup for different Aperture diameters at the receiver where $C_n^2 = 3.24 \times 10^{-14}$.	88
4.17	BER rate for strong turbulence measurements in UMD setup for different Aperture diameters at the receiver where $C_n^2 = 3.24 \times 10^{-14}$.	88
4.18	SNR rate for strong turbulence measurements in UMD setup for different Aperture diameters at the receiver where $C_n^2 = 9.59 \times 10^{-14}$.	89
4.19	BER rate for strong turbulence measurements in UMD setup for different Aperture diameters at the receiver where $C_n^2 = 9.59 \times 10^{-14}$.	89
4.20	SNR vs. C_n^2	90

List of Tables

2.1	C_n^2 values for each class	31
2.2	Success Rate and Feature Dimensions for each scenerio	32

Babaannem'e ..

Chapter 1

INTRODUCTION

1.1 Overview of Turbulence

Free Space Optical (FSO) Communication Links otherwise known as Optical Wireless Communication (OWC) Systems use the atmosphere as the communication channel. The power density of the laser beam is reduced mainly due to scattering and molecular absorption. Changes in atmospheric conditions change the refractive index distribution in the air. It changes the propagated beam temporarily in an unpredicted way in its phase front and total power received. Additionally it has been shown that the presence of fog may completely eliminate the passage of the optical beam [1]

Absorption and scattering effects generally cause attenuation in the beam. Refractive index fluctuations in atmosphere lead to irradiance fluctuations, beam broadening and the loss of spatial coherence of the optical wave, among other effects. Eddies with scale sizes larger than the beam diameter cause beam wander whereas scale sizes that are on the order of first Fresnel zone ($\sqrt{L/k}$) are primarily the cause of irradiance fluctuations (scintillations). Clearly these strong

effects have major consequences on optical information systems used in astronomical imaging, optical communications, remote sensing, laser radar etc. that require transmission of optical waves through the atmosphere.

The theory of optical propagation through the atmosphere essentially have different explanations according to the strength of turbulence regime. The most important parameter for the success of comparison with experimental data is the weather conditions of the experimental sight. Therefore, it's important to know more about the structure of the atmosphere itself.

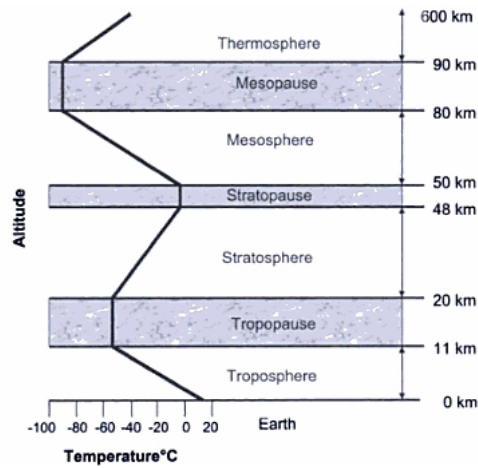


Figure 1.1: Atmospheric Layers. Source: *Larry C. Andrews, Laser Beam Propagation Through Random Media, pg:10*

The atmosphere is a gas envelope that covers the earth. It is divided into 4 primary layers and 3 isothermal boundaries. The Troposphere layer contains 75% of the earth's atmospheric mass and maximum air temperature occurs in the near surface of the earth. The tropopause layer is an isothermal layer where the air temperature remains constant at -55°C . In the Stratosphere layer, the air temperature increases with altitude because of the effect of ozone where the absorbed sunlight creates heat energy. The Stratopause boundary creates an isolation layer between Mesosphere and stratosphere layers. In the Mesosphere layer, the temperature is relatively cooler and it decreases down to -90°C . The Mesopause boundary is a third isothermal boundary. Finally the air temperature

in the Thermosphere layer rises significantly after 90 km and it also contains most of the Ionosphere and Exosphere. The layers of atmosphere can be seen in Figure 1.1.

All of the experiments done in this thesis have been done in the Troposphere layer, where most of the atmospheric mass is carried and most of the life we know exist.

Absorption and scattering generally refer to wavelength dependent attenuation of electromagnetic radiation where in absorption, atmospheric molecules absorb energy from incident photons and in scattering, photons collide with the atmospheric molecules. In the atmosphere, H_2O , CO_2 , CO , NO_2 , and the ozone are the fundamental absorbers. Little absorption occurs at visible wavelengths ($0.4 - 0.7 \mu m$) except for H_2O absorption between $0.65 \mu m$ and $0.85 \mu m$. First order scattering, known as Rayleigh law, is caused by air molecules that are relatively smaller than the wavelength of the radiation. The scattering coefficient is proportional to λ^{-4} , known as the Rayleigh Law. Mie Scattering is scattering with particles comparable in size to the radiation wavelength. Losses from scattering decrease abruptly as the wavelength increases.

Overall, the transmittance of a laser beam that has propagated a distance L through the atmosphere can be interpreted with the Beer's Law :

$$\tau = \exp[-\alpha(\lambda)L] \quad (1.1)$$

where, $\alpha(\lambda) = A_a + S_a$, A_a : Attenuation coefficient and S_a : Scattering coefficient and $\alpha(\lambda)L$ is the optical depth.

As a result of some of the software packages that are commercially and freely available, we can derive the transmittance effects of a horizontal path in the atmosphere as a function of wavelength as it can be seen in Figure 1.2. In classical theory of turbulence, atmosphere is defined in two distinct states of motion, laminar and turbulent. In laminar flow, mixing of the media does not

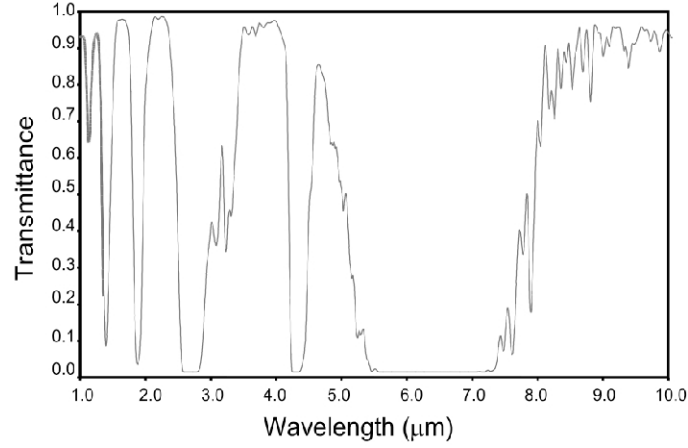


Figure 1.2: Typical atmospheric transmittance for 1 km horizontal path, 3 meters above the ground, no fog, no rain, no clouds. Source: *Larry C. Andrews, Laser Beam Propagation Through Random Media, pg:13*

occur and velocity flow characteristics of media change in a regular fashion. In turbulent flow, dynamic mixing of the media occurs and velocity flow loses its uniform characteristics. As a result of the dynamic mixing of turbulent flow random sub-flows called turbulent eddies are created. The theory assumes the small scale structure of turbulence to be statistically homogeneous, isotropic, and independent of larger scale structure.

The source of energy at larger scales is either wind shear or convection. In cascade theory of turbulence, when the wind velocity reaches a critical point, it creates unstable air masses (eddies) that are slightly smaller and independent from the initial flow. So larger eddies break up into smaller eddies and form a continuum of eddy sizes between the L_o (outer scale of turbulence) and l_o (inner scale of turbulence). An illustration is shown in Figure 1.3.

1.2 Classical Theory

In classical theory of optical wave propagation, the assumption is essentially unbounded continuous medium with smoothly varying refractive index. Therefore

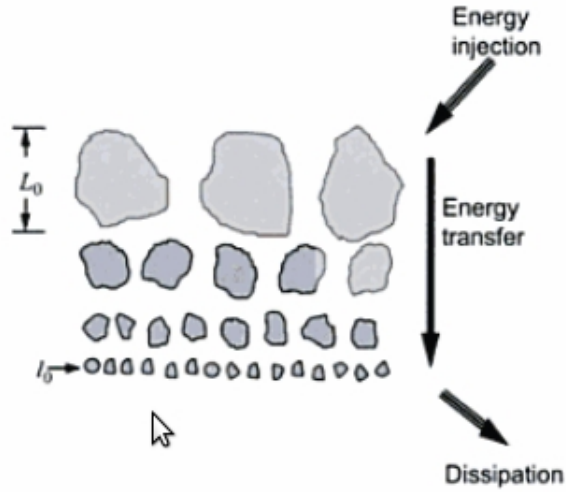


Figure 1.3: The Cascade theory of turbulence where L_o denotes the outer scale and l_o is the inner scale. Source: *Larry C. Andrews, Laser Beam Propagation Through Random Media, pg:60*

assuming a monochromatic wave, the vector amplitude of the field can be described by Maxwell's equations [2],

$$\nabla^2 E + k^2 n^2(R)E + 2\nabla[E \cdot \nabla \log(n(R))] = 0; \quad (1.2)$$

where $R = (x, y, z)$ denotes a point in space and $k = 2\pi/\lambda$ is the wave number of the electromagnetic wave, λ is the wavelength and $n(R)$ is the refraction index.

The main starting point for the classical theory of propagation through random media is [2],

$$\nabla^2 U + k^2 n^2(R)U = 0 \quad (1.3)$$

where $U(R)$ is the scalar component of the electric field. Essentially all approaches for solving this equation rely on the following fundamental assumptions [2],[3],[4]:

- Depolarization effects can be neglected.

- Backscattering of the wave can be neglected.
- The wave equation may be approximated by the parabolic equation.
- The refractive index is dirac delta correlated in the direction of propagation.

The first method that agrees with the experimental data is the Rytov approximation using *log – normal* model for irradiance. The starting point for this method is given below.

$$U(R) \equiv U(r, L) = U_0(r, L)e^{\psi_1(r, L) + \psi_2(r, L) + \dots} \quad (1.4)$$

where $U_0(r, L)$ is the unperturbed field and $\psi_1(r, L)$ and $\psi_2(r, L)$ represent first and second order perturbations. These perturbations are explained in the normalized Born Approximations according to,

$$\psi_1(r, L) = \frac{U_1(r, L)}{U_0(r, L)} = \Phi_1(r, L), \quad (1.5a)$$

$$\psi_2(r, L) = \frac{U_2(r, L)}{U_0(r, L)} - \frac{1}{2} \left[\frac{U_1(r, L)}{U_0(r, L)} \right]^2 = \Phi_2(r, L) - \frac{1}{2} \Phi_1^2(r, L). \quad (1.5b)$$

It is interesting that even though all of the approximations that are used in Rytov theory are taken from Born approximation and Born approximation is only a way to explain extremely weak turbulence conditions, the three integrals that are given below are used to explain second and fourth order statistics in the theory of propagation through random media, where $\Phi_n(K, z)$ shows the n^{th} order spectral representation.

$$\begin{aligned} E_1(0, 0) &= \langle \psi_2(r, L) \rangle + \frac{1}{2} \langle \psi_1^2(r, L) \rangle \\ &= -2\pi^2 k^2 \int_0^L dz \int_0^\infty dK K \Phi_n(K, z) \end{aligned} \quad (1.6)$$

$$\begin{aligned}
E_2(r_1, r_2) &= \langle \psi_1(r_1, L) \psi_2^*(r_2, L) \rangle \\
&= 4\pi^2 k^2 \int_0^L dz \int_0^\infty dK K \Phi_n(K, z) J_0(K|\gamma r_1 - \gamma^* r_2|) \\
&\times \exp\left[-\frac{iK^2}{2k}(\gamma - \gamma^*)(L - z)\right],
\end{aligned} \tag{1.7}$$

$$\begin{aligned}
E_3(r_1, r_2) &= \langle \psi_1(r_1, L) \psi_1(r_2, L) \rangle \\
&= 4\pi^2 k^2 \int_0^L dz \int_0^\infty dK K \Phi_n(K, z) J_0(\gamma K|r_1 - r_2|) \\
&\times \exp\left[-\frac{iK^2 \gamma}{k}(L - z)\right],
\end{aligned} \tag{1.8}$$

1.3 Aperture Averaging Theory

Decrease in scintillation with the increase in the receiver lens area is known as Aperture Averaging(AA). The decrease in scintillation due to aperture averaging can be reached from the ratio of power fluctuations over a defined size of aperture by a point size aperture. Assuming $I(r, L)$ is the irradiance of an optical wave collected by a lens of a receiver diameter D in an FSO system, L is the propagation distance and r is the spatial vector in the transverse plane of the receiving lens, then the total power that is collected from the receiver lens $P = \int I(r, L) dr$.

If we are dealing with an unbounded plane wave,

$$\langle P \rangle = \frac{1}{8} \pi D^2 \langle I \rangle \tag{1.9}$$

where $\langle I \rangle$ is the mean irradiance. The normalized variance of power fluctuations in the receiver plane leads to[5],

$$\begin{aligned}
\sigma_p^2(D) &= \frac{\langle P^2 \rangle - \langle P \rangle^2}{\langle P \rangle^2} \\
&= \frac{16}{\pi D^2} \int_0^D b_I(p) \left[\cos^{-1}\left(\frac{p}{D}\right) - \frac{p}{D} \left(1 - \frac{p^2}{D^2}\right)^2 \right] p dp,
\end{aligned} \tag{1.10}$$

where $b_I(p) = B_I(p)/B_I(0)$ is the normalized covariance of irradiance fluctuations, p denotes the separation distance between two points on the wavefront and the terms in the brackets arise from the optical transfer function or the Mutual Transfer Function (MTF). The covariance function of the irradiance is

based on the assumption of the modulation process $I = xy$ and the irradiance covariance function can be expressed as the sum,

$$B_I(p) = B_x(p) + B_y(p) + B_x(p)B_y(p) \quad (1.11)$$

where $B_x(p)$ is the covariance of the large-scale fluctuations and $B_y(p)$ is the covariance of the small-scale fluctuations.

In the literature, the covariance of irradiance can also be expressed as [2][3][4],

$$B_I(p) = e^{B_x(p)+B_y(p)} - 1 . \quad (1.12)$$

Under weak turbulence regimes, the correlation width of the optical scintillation screen is on the order of the Frensel zone $\sqrt{L/k}$ [6]. However as the strength of the turbulence gets bigger, the correlation length decreases. When the long residual correlation length is considered, it is found that the correlation length can be determined by the scattering disk size $\frac{L}{kp_0}$, p_0 being the spatial correlation length under strong turbulence regimes [3].

In this thesis, numerous studies are done in atmospheric optics to investigate the nature of turbulence. In chapter 2, we are focusing on several subjects; turbulence strength estimation from sequential images taken as output of a large aperture telescope, simulation of propagation of a turbulence induced beam in various turbulence regimes using phase screen method, turbulence strength estimation using angle of arrival method, image acquisition algorithm which is especially useful in strong turbulence induced images and Support Vector Machine (SVM) algorithm for estimating turbulence strength in weak to moderate turbulence conditions. In chapter 3, a turbulence investigation setup has been proposed and weak to strong turbulence induced beam has been investigated in various experiment sites and weather conditions. In addition, a feasible and practical method for turbulence strength estimation setup has been proposed. In

chapter 4, the experimental results that are gathered in weak to strong turbulence regime has been compared with the scintillation index theory, which is the most accepted theory that is in use in experimental and theoretical studies in atmospheric turbulence literature. It is seen that although there is a very good correlation with the data taken in weak to moderate regime, as the turbulence level gets stronger the error margin increases. So the literature is in need of a superior theory that will explain intensity variations of a given receiver aperture in all turbulence regimes.

Chapter 2

Simulation Model

2.1 Refractive Index Structure Constant (C_n^2) Evaluation

In turbulence theory, the fundamental problem with the processing of the image sequences is the measurement time that takes place within the turbulent media. Estimating turbulence strength that is resulted by intensity fluctuations in a turbulent media is yet another challenge to get over. The path-averaged refractive index structure constant, C_n^2 , is a fundamental parameter to characterize the atmospheric turbulence. In order to measure C_n^2 , we need a device called a scintillometer which processes the image in real time and needs expensive equipments. In this part of the thesis, we want to present a method to estimate the C_n^2 parameter from a turbulence induced image sequence.

Random variations in the refractive index induce multiple refractions to the wave propagating through the atmosphere. So the wave front propagating through arrives at the output plane with random phase angles whose variances

depend on the strength of the turbulence. This phenomenon has two main impacts at the output plane. The first one is the spatiotemporal movements in the image plane. In the practical case, the same intensity value occurs in different pixel locations across the frames. The distance between each location is directly related with the turbulence strength and a method will be presented to measure the C_n^2 parameter. The second one is the long exposure blur. Long exposure blur is caused by the technique that is being used when capturing images with a camera. In a sufficiently short time exposure (up to a few milliseconds), the intensity of a single wave front with random angle of arrival can be recorded at each frame. But the cameras with sufficiently long exposure times will simply add the intensities of the wave fronts and integrate over time. So simply, the effect of 'angle of arrival' will be averaged over the spatial domain and we will lose the knowledge of spatiotemporal movements occurring in the propagation direction.

Assuming that we have a camera with sufficiently short exposure time, the variance for turbulence induced plane wave assuming path averaged C_n^2 is given as [7],

$$\sigma_a^2 = D^{-1/3} C_n^2 L \times P \quad (2.1)$$

where,

$$P = \begin{pmatrix} 2.914, l_0 \ll D \ll \sqrt{\lambda L} \\ 1, 1, \sqrt{\lambda L} \ll D \ll L_0 \end{pmatrix}$$

A wave front angular shift at α radians results in an image displacement of $\alpha x PFOV^{-1}$ where PFOV is the pixel field of view. So the image displacement in a spatial domain for the output plane is,

$$\sigma_{img}^2 = \sigma_a^2 PFOV^{-2} . \quad (2.2)$$

By filtering the image with gradient based masks, we can have the changed images in both spatial axes. A spatiotemporal, 4-point central difference for differentiation (with mask coefficients) $1/12(-1,8,0,-8,1)$ has been used as a mask.[3] The strength of the change is derived mostly from the size of turbulence eddies and it is directly proportional to the intensity variance as [8],

$$\sigma_I^2(m, n) = [I_x^2(m, n) + I_y^2(m, n)]\sigma_{img}^2 \quad (2.3)$$

where $I_x(m, n)$ and $I_y(m, n)$ represent the pixel location of gradient filter result.

So overall, the intensity variance can be calculated as,

$$\sigma_I^2(m, n) = [I_x^2(m, n) + I_y^2(m, n)]D^{-1/3}C_n^2 \times L \times P \times PFOV^{-2} \quad (2.4)$$

The C_n^2 parameter can be obtained as,

$$C_n^2(m, n) = ([I_x^2(m, n) + I_y^2(m, n)] \times L \times P)^{-1}PFOV^2D^{1/3}\sigma_I^2(m, n) \quad (2.5)$$

At the end we have found a C_n^2 value for each pixel of the output image. The average is the estimated turbulence strength parameter,

$$C_n^2 = \frac{\sum_{m,n} C_n^2(m, n)}{m \times n} \quad (2.6)$$

The C_n^2 image that is seen in Figure 2.1 represents the change in the refractive index along the pixel path. It is observed that the results occur where the image intensity lies.

For further investigations, a scintilometer is needed to run simultaneously with our setup as we gather images. Comparing the estimated values and the gathered ones from the scintilometer will give us a chance to make a perfect estimation.

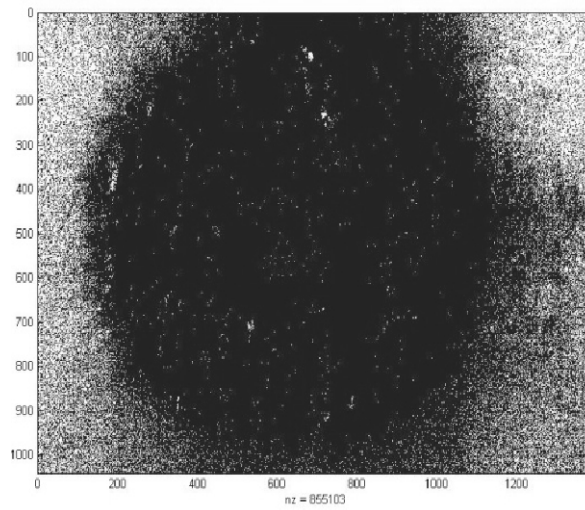


Figure 2.1: The C_n^2 image where the refractive index fluctuations occurs

2.2 Phase Screen Method

2.2.1 Introduction

Experimenting on a free space optical communication system is rather tedious and difficult. The interferences of plentiful elements affect the result and cause the experiment outcomes to have bigger error variance margins than they suppose to have. Especially when we go into the stronger turbulence regimes, the simulation and analysis of the turbulence induced beams require delicate attention [9]. Simulation of the beam propagation through a turbulent media for diverse turbulence regimes is investigated in our previous studies [10].

For all of these purposes, a method for creating turbulence effects on a propagated beam in a desired experimental condition for all turbulence regimes is presented in this section.

In our simulations, we have used a point source which combines the Gaussian and sinc forms in 2D [11] [12],

$$p_{gausSinc} = \exp(-j \frac{k}{2D_z} r^2) \frac{D_{ob}}{\lambda D_z} \text{sinc}(\frac{D_{ob}}{\lambda D_z} x_1) \text{sinc}(\frac{D_{ob}}{\lambda D_z} y_1) \quad (2.7)$$

where D_z is the propagation distance x_1, y_1 are the cartesian spatial coordinates, r is the polar spatial coordinate and D_{ob} is the diameter of the observation field aperature.

In the act of propagation through air, a super-Gaussian absorbing boundary is applied spatially through for addition of random phase screens to the propagated beam [13]. It is useful for getting rid of the back reflections from boundary layer in propagation between two phase screens.

$$G_{SupG} = \exp(-\frac{1}{2}(\frac{r}{\sigma})^8) \quad (2.8)$$

where r is the location parameter of polar coordinates and σ is about the half of the number of grids (N).

For the propagation of the beam, the angular spectrum form of Fresnel diffraction has been used [11],

$$U(r_2) = F^{-1}[r_2, f_1]\{H(f_1)F(f_1, r_1)\{U(r_1)\}\} \quad (2.9)$$

where $F[r, f]$ is the fourier transform and $H(f)$ is the transfer function of the free space propagation given as,

$$H(f_1) = e^{jk\Delta z} e^{j\pi\lambda\Delta z(f_{x_1}^2 + f_{y_1}^2)} \quad (2.10)$$

The modified Von Karman spectrum has been chosen for its identity with the Kolmogorov spectrum when the inner scale of turbulence, $l_0 = 0$ and outer scale of turbulence $L_0 \cong \inf$,

$$PSD_{modVonKar} = 0.033C_n^2 \exp(-\frac{(\frac{K}{K_m})^2}{(\frac{K^2}{K_0^2})^{\frac{11}{6}}}) \quad (2.11)$$

where $K_m = \frac{5.92}{l_0}$ and $K_0 = \frac{2\pi}{L_0}$

In Figure 2.2, the Modified Von Karman Spectrum vs the Von Karman Spectrum is given. Experimental results show that the bump near $1/l_0$ is steeper for the modified version of the Von Karman Spectrum so we choose it in our simulation.

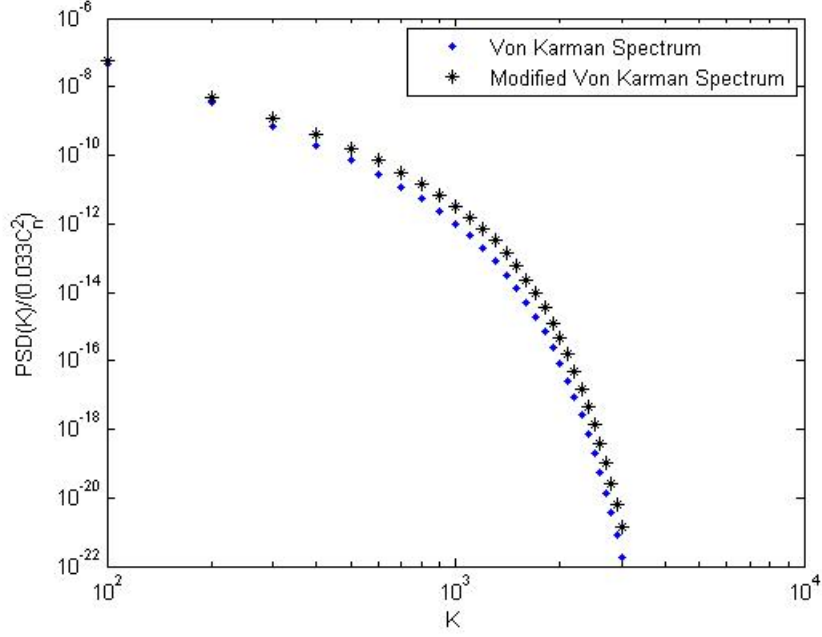


Figure 2.2: Modified Von Karman Spectrum vs the Von Karman spectrum

2.2.2 Phase screen Methodology

Simulation of the beam propagation in a turbulent media is explained in the literature [11] [12] [14] [15]. In the preceding section, we offer a methodology for creating real-time turbulence like atmospheric effects on a propagated beam with a predetermined turbulence strength.

Using the point source in the form of Eq. 2.7, we have established a propagation pattern at a distance D_z . After defining equi-distance observation plane locations between the source plane and the final observation plane, the same numbers of turbulence phase screens have been created to alter the phase factor of the propagated beam. The methodology for the turbulence phase screen is described in the following paragraphs.

Fast fluctuations, which are found to be the effective parameter that cause the strong turbulence, are applied to the propagated beam for each screen defined

by the Fresnel diffraction method where Δ_{ob} is the observation plane spacing and the N is FFT factorization number.

Depending on the observation grid spacing, the frequency grid is also established,

$$f_{fast} = (-N/2 : N/2 - 1) \times \frac{1}{N \times \Delta_{ob}} \quad (2.12)$$

Using Eq. 2.11, we have calculated the associated power that is induced by the fast fluctuations where $K = \frac{2\pi}{\lambda_{fast}}$ and $\lambda_{fast} = \frac{c}{f_{fast}}$.

In the forthcoming section, we are offering a new method for calculating the power spectrum for both slower and faster fluctuations. For turbulence regimes that are moderate to strong ($\sigma_R > 1$), we believe that variations of the power fluctuations that are induced to the propagated beam gets bigger. So in the process of calculation of the power associated with each turbulence phase screen, the C_n^2 variation increases even after short distances. By taking the effect of the angular spectrum form of Fresnel diffraction into account (Eq.2.9), we introduce randomness to the power that is induced to the propagated beam in each turbulence phase screen which will be effective in reaching the desired turbulence strength.

First a initial C_n^2 has been decided for the specific propagation path and turbulence regime. Then the C_n^2 function for all turbulence regimes is introduced for each phase screen as,

$$C_{nScr n} = randn(C_n^2, C_n^2 \times \frac{\sigma_R^2}{100}) \quad (2.13)$$

where *randn* is a matlab function that generates a normal distributed random number with a mean of C_n^2 and a variance of $C_n^2 \times \frac{\sigma_R^2}{100}$.

Then normal distributed random numbers with a unity power of $(N \times N)$ size phase screen is created. For each phase screen along the propagation path, power associated for each pixel point is assigned to the appropriate planar frequency as a Fourier coefficient of the phase screen according to the power spectrum density calculated in Eq. 2.12. So at the end, we have introduced randomness not only in the spatial and temporal domains but also in the power associated with turbulence in each phase screen.

$$c_{nFast} = rand[N \times N] \times \sqrt{PSD_{fast}} \times \Delta_{ob} \quad (2.14)$$

The Inverse Fourier transform is taken in 2D for realizing the fast fluctuation effect of the turbulence phase screen Φ_{high} ,

$$\Phi_{high} = F^{-1}\{c_{nFast}\} \quad (2.15)$$

Resulted fast fluctuations can be seen in Figure 2.3.

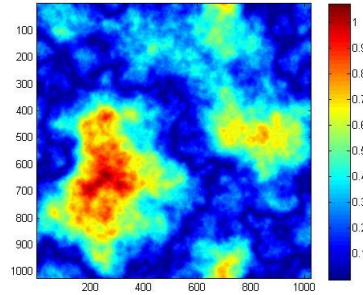


Figure 2.3: Fast Fluctuation Effect of the Optical turbulence on a 100 meter slant path with a $C_n^2 = 10^{-16}$.

Lower fluctuations have been accomplished using the same rule applying a larger frequency grid,

$$f_{low} = [-1, 0, 1] \times \frac{1}{3^{round(3.4/(C_n^2 \times 10^{16}))} \times N \times \Delta_{ob}} \quad (2.16)$$

Again using Eq. 2.11, we have calculated the associated power that is induced by the lower fluctuations where $K = \frac{2\pi}{\lambda_{low}}$ and $\lambda_{low} = \frac{c}{f_{low}}$.

Then the Fourier coefficients associated with the lower fluctuations are calculated by,

$$c_{nLow} = rand[N \times N] \times \sqrt{PSD_{Low}} \times \Delta_{ob} \quad (2.17)$$

And the turbulence phase screen for lower fluctuations is found by taking an inverse Fourier transform,

$$\Phi_{Low} = F^{-1}\{c_{nLow}\} \quad (2.18)$$

Resulted fast fluctuations can be seen in Figure 2.4,

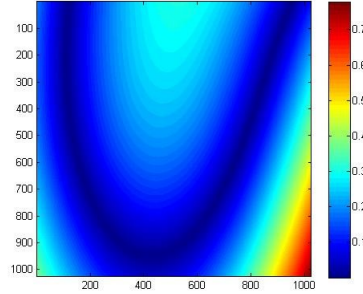


Figure 2.4: Lower Fluctuation Effect of the Optical turbulence on a 100 meter slant path with a $C_n^2 = 10^{-16}$.

The addition of the two effects have created a practical turbulence screen with pre-known turbulence structure parameter (C_n^2) according to Eq. 2.19 and is given in Fig. 2.5. Using this type of addition for each phase screens we are giving a major role to the fast fluctuations in strong turbulence regimes whereas in weaker turbulence regimes this role goes to the lower fluctuations [10].

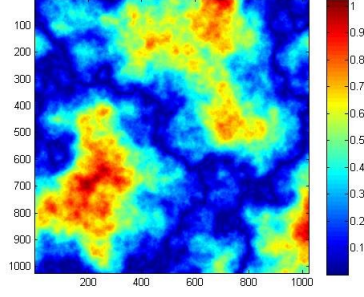


Figure 2.5: Simulation Result of Optical turbulence screen on a 100 meter slant path with a $C_n^2 = 10^{-16}$.

$$\Phi_{TOT} = \Phi_{Fast} \times e^{-\sigma_R^{-1}} + \Phi_{Low} \quad (2.19)$$

Resulted optical turbulence screen have been collimated with each sequential observation plane. The influence of the turbulence phase screen has been passed through, while we propagate using Eq. 2.9 until the last observation plane.

2.2.3 Results

We have a perfect scintillation pattern which has a specific turbulence strength structure constant (C_n^2) with a pre-defined propagation distance. In Figures 2.6-2.7, we can see the observation plane of a 633 nm beam after 100 meters of distance in various turbulence strengths.

The simulation results of the Aperture Averaging factors for varying Aperture Sizes in various turbulence regimes is given in Fig. 2.8. The strong turbulence data shows itself in the saturation level of the Aperture Averaging Factor.

The experimental results and their methodology has been explained throughout Chapter 3. Experimental and simulated results of Point Averaged Aperture Averaging (PAAA) Factor for the strong turbulence regime is given in Fig. 2.9. Experimental results in the strong turbulent regime show us that the declination

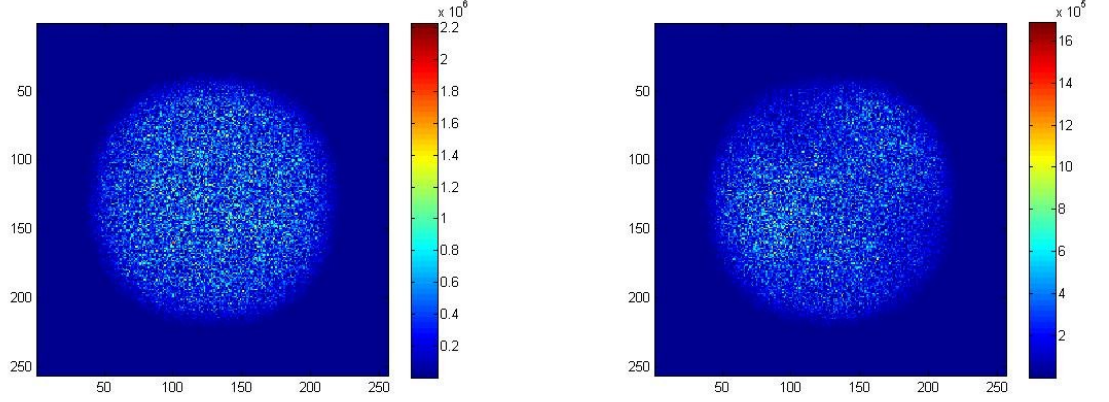


Figure 2.6: Strong Turb. ($C_n^2 = 10^{-10}$) and Intermediate Turb. ($C_n^2 = 10^{-13}$) Images, Path:100 m. $l_0 = 5mm$ and $L_0 = 10^4$.

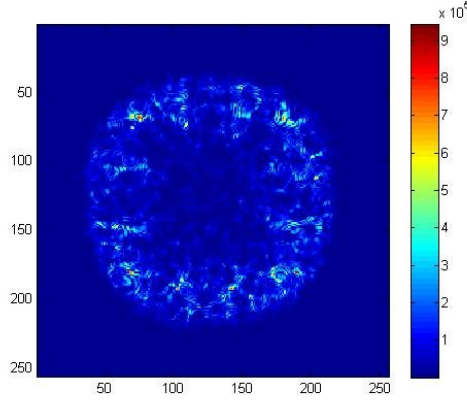


Figure 2.7: Weak Turb. Image, Path:100 m. $C_n^2 = 10^{-15}$, $l_0 = 5mm$ and $L_0 = 10^4$.

of the curve is very similar to our simulation results. There is a %10 error margin in the saturation region of the Aperture Averaging curve which is acceptable in strong turbulent regimes.

The AA Factor for weak-to-moderate turbulence regime is given in Fig. 2.10. Experimental results seem to match up with the simulation results in the saturation regime of the curve. It is our idea that the declination difference is caused by the number of phase screens that are in use. The difference can be decreased

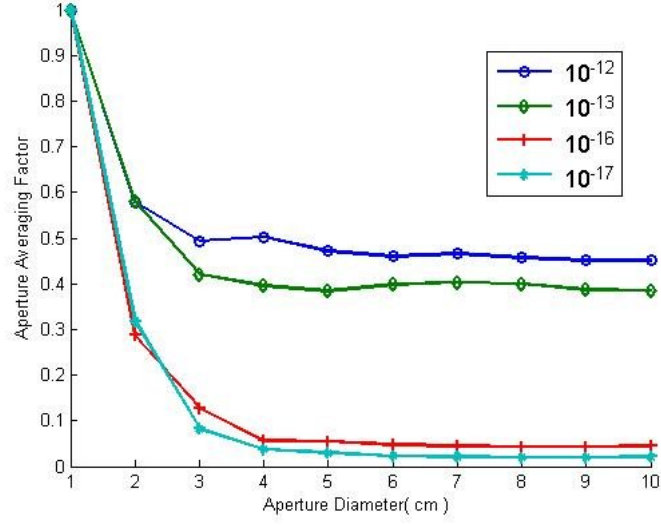


Figure 2.8: Simulated Aperture Averaging Results over 100 meters for various C_n^2 values

by increasing the number of sampling we take from the observation plane for each realization.

In conclusion, a practical method for creating turbulence like phase screens has been established in desired turbulence regimes. The new method for establishing the right measures of addition to the propagated beam has been constructed by arranging the influence of lower and faster fluctuations. It has been found that faster fluctuations are more effective on the strong turbulent regimes. Desired turbulence strength has been established with simulation by suggesting temporal fluctuations in the induced turbulence power in strong turbulence conditions.

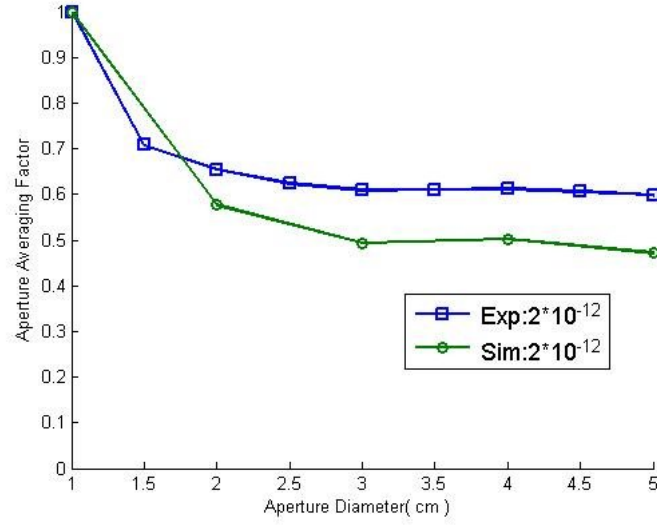


Figure 2.9: Experimental and Simulated Results of the Point Averaged Aperture Averaging Factor for $C_n^2 = 2 \times 10^{-12}$, path length = 120 meters, $l_0 = 5 \text{ mm}$ and $L_0 = 10^4$.

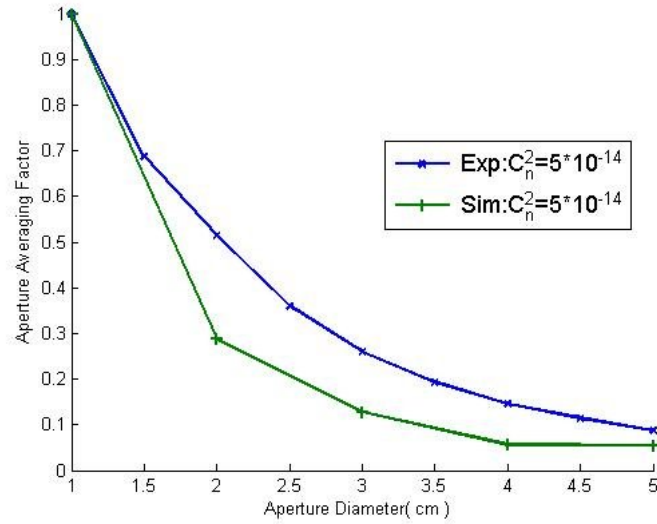


Figure 2.10: Experimental and Simulated Results of the Point Averaged Aperture Averaging Factor for $C_n^2 = 5 \times 10^{-14}$, path length = 120 meters, $l_0 = 5 \text{ mm}$ and $L_0 = 10^4$.

2.3 Image Acquisition and Tracking Algorithm

The ideal image at the receiver side without any turbulence should be seen as a perfect donut shape(Fig. 2.11). In terms of intensity distribution, we can safely approximate the same intensity value at each point (plane wave approximation) since $D \ll \sqrt{\lambda}L$, where D is the receiver aperture, λ is the wavelength and L is the propagation path. Existing data from the University of Maryland setup have been used to test our software.

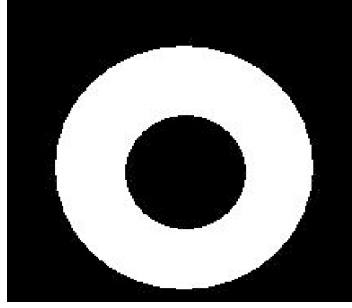


Figure 2.11: Intensity Distribution of the Image at the Receiver Side with no Turbulence Effects.

The dark area occurs in the middle because of the small diameter mirror of the Schmidt-Cassegrain telescope at the receiver side blocking the central portion of the image as shown in Figure 2.12.

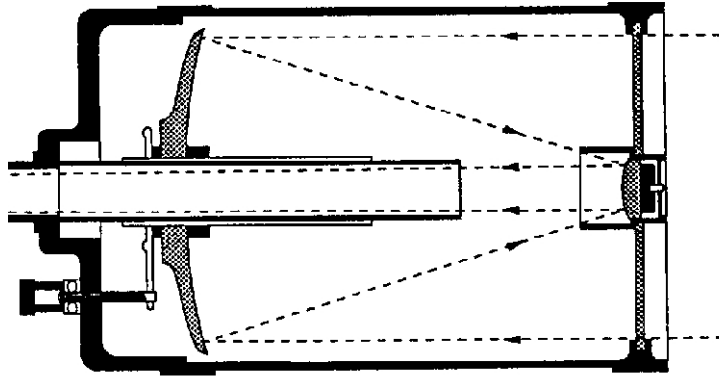


Figure 2.12: The view of the light path in the optical design of the telescope

Due to turbulence induced fluctuations, the intensity distribution of the image at the receiver becomes rather plain and simple as shown in Figure 2.13. Resulted boundaries as a result of the software is shown in Figure 2.13. In order to analyze the image, we have to set some deterministic boundaries for where our information lies. Mainly we can determine these boundaries by only two parameters, radius of the inner circle and radius of the outer circle. The preceding method will explain the steps of succession in our software.

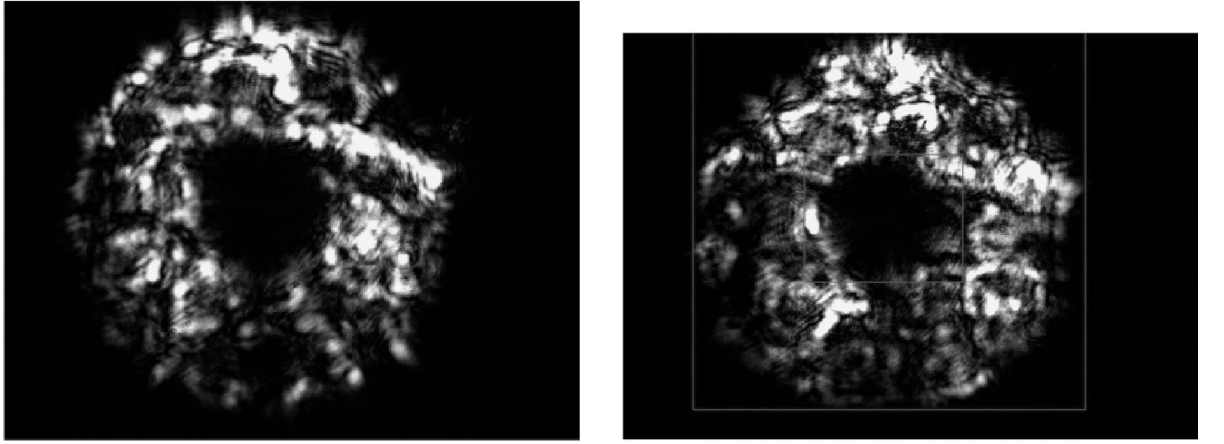


Figure 2.13: Turbulence induced image and Region result of the software

At first, we subtract the background noise, which is only one frame that is taken from the camera when the laser is off, caused by the noise that is coming from thermal radiations or sun rays. After that process, a smoothing operation is needed to reduce the effects of the turbulence generated paths from the inner circle to the outer circle. Examples of such images can be seen in Figure 2.14.

Then we convert a binary image from the result to see where our information lies. Smoothing operation gives us a better understanding of the inner and outer boundaries of the image. The difference caused by the smoothing operation can be clearly seen in Figure 2.15.

Labeling each of the closed boundaries gives us several regions inside our image matrix. The biggest one of these should be able to give us the outer

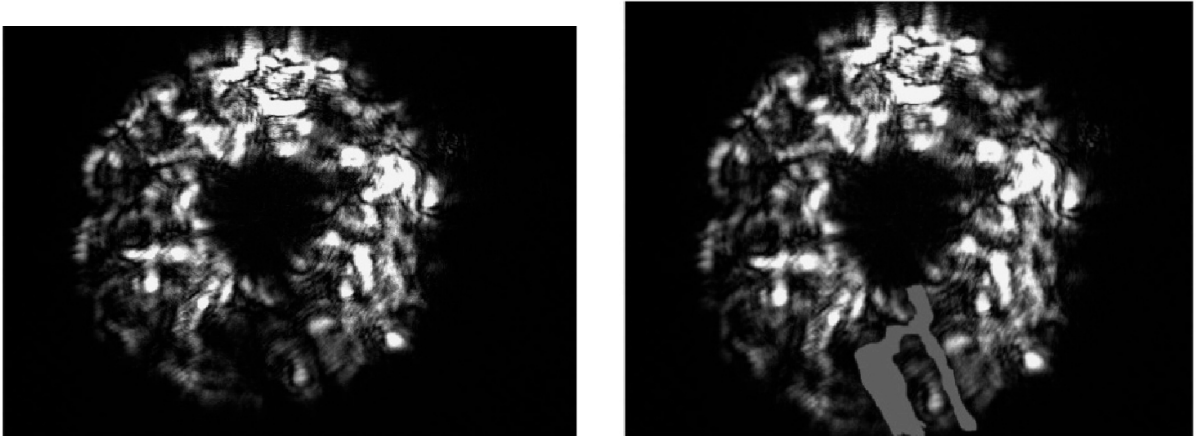


Figure 2.14: Turbulence induced problematic image and the Region that is causing problems

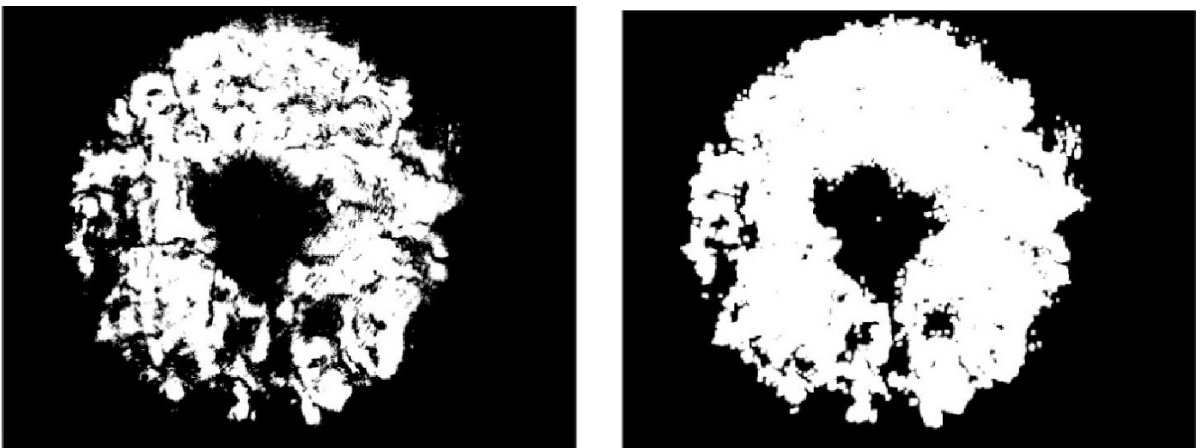


Figure 2.15: Binary image without smoothing and Binary image after smoothing

radius of the image. For the region with the biggest area, we are able to fit a square or a circle after that by calculating the minimum and maximum location points in the x-axis and the y-axis.

The same operation applies for the inner circle. The only difference is that the region of the inner circle is assumed to be higher than $1/8$ of the size of the image.

Once the inner and outer radius of the captured frames are determined, the same framing technique discussed previously is used in calculating the Aperture

Averaging Factor. The better masking technique discussed above produced more efficient Aperture Averaging Factor results.

2.4 Analysis of turbulence strength for free space optical communication using Support Vector Machine (SVM) regression methods

2.4.1 Introduction

Free space optical(FSO) communication links have become more and more important in recent years. They provide high speed, secure point to point communication. They have low probability of interception and low probability of detection. And of course they are favorite with their rapid deployment and flexible properties. The most favorite property of these systems is they are much more cheaper in comparison with to its alternative fiber optic communication links.

Unfortunately the only problem in the FSO Links is in the turbulence that occurs in the channel that is the atmospheric space between the transmitter and receiver. Accordingly, the modulation scheme changes in the sense of increasing the redundancy which reduces the bandwidth of the communication system. The optimum communication speed can only be decided by knowing the model of turbulence. Different models for optical transmission in different turbulence regimes exist in the literature [16]. But they all depend on a parameter, C_n^2 , which basically gives us information about the strength of the turbulence.

The refractive index structure function, C_n^2 , is a parameter which describes the magnitude of the turbulence effects in the atmosphere for the optical range. In order to measure it, we need a device called a scintillometer which processes the information realtime and needs expensive optical equipments. In this study, we will try to estimate C_n^2 from different strengths of turbulence induced images using support vector regression methods.

2.4.2 Feature Extraction

The data consists of 10 classes with 30 patterns in each class with weak-to-strong turbulence C_n^2 values. Our patterns are the images we got from our outdoor optical setup. The images are obtained by a CCD camera with a 1ms shutter speed which allows us to get the required power in our camera without much of intensity saturation. Each image has 1040 x 1393 pixels. So it is not computationally sensible to use all of the image as our feature vector. Therefore, different methods are applied in the proceeding sections.

2.4.3 Region Covariance Method

Feature selection is a critical step for classification problems. Region covariance is a fast method and has efficient algorithm. In this method, the covariance of some statistics of the image is obtained and the elements of that covariance matrix are used as features. Note that, it is assumed that covariance is enough to discriminate two different distributions. Note also that two distributions with different means but the same covariance matrices will not be classified. However, this is very unlikely to occur in practice [17]. Since the covariance is used for the feature selection, the dimensionality is reduced considerably. Due to symmetry, the covariance matrix has only $d(d + 1)/2$ different elements, where d is the number of dimension for each frame that belongs to a specific class. On the other hand, the raw values need $(n \times d)$ dimension which is much larger, where n is the number of frames in each class. In order to obtain the covariance matrix, pixel locations (x, y) and the first order and second order derivatives are used as the elements of the feature vector. Therefore, each pixel of the image is represented by a seven-dimensional feature vector given as [17],

$$F(x, y) = [x \ y \ R(x, y) \ |\frac{\partial I(x, y)}{\partial x}| \ |\frac{\partial I(x, y)}{\partial y}| \ |\frac{\partial^2 I(x, y)}{\partial^2 x}| \ |\frac{\partial^2 I(x, y)}{\partial^2 y}|] \quad (2.20)$$

where (x, y) is the pixel location, R is the color value and I is the intensity. The image derivatives are calculated using the filters $[1 \ -1]^T$ and $[-1 \ 2 \ -1]^T$ for the first order and second orders respectively. Therefore, the covariance is obtained as a 7x7 matrix with 28 different elements. Note that, the feature can be reduced by excluding second order derivatives given in equation (2.20). In this case, the covariance matrix is obtained with 5x5 dimensions and the number of different elements is reduced to 15. In our study, the features are extracted for both cases and the results are discussed.

2.4.4 Discrete wavelet transform (DWT)

In Discrete Wavelet Transform (DWT), unlike the Fourier transform, the signal is represented in time-frequency domain. In DWT, there is a set of basis functions, called wavelet, that replace sinusoidal basis functions in the Fourier transform. The wavelets are stretched and shifted version of a fundamental real valued wavelet (mother wavelet) [18]. A wavelet is defined by a wavelet function and scaling functions. The wavelet transform is considered as very useful since they provide an efficient representation of many type signals. In this study, 1-level and 3-level wavelet transforms are applied to each image and the energy of multi-level decomposed image is used as the features. The standard deviation can be computed as [19],

$$\sigma_k = \sqrt{\frac{1}{MxN} \sum_{i=1}^M \sum_{j=1}^N (w_k(i, j) - \mu_k)^2} \quad (2.21)$$

where w_k is the coefficient of k th multiwavelet decomposed sub-band, μ_k is the mean value of the k^{th} sub-band and $M \times N$ is the size of multiwavelet decomposed sub-band.

2.4.5 Complex Wavelet Transform

Despite its efficient computational algorithm, wavelet transforms have some shortcomings such as oscillations, shift variance, aliasing and lack of directionality. Instead, dual-tree complex wavelet transform which overcomes this limitations can be considered [18]. In this method, the complex transform of a signal is calculated using two different DWT decompositions and six *sub-bands* are produced at each scale. In this study, 2D-dual tree complex wavelet transform is applied and the features are extracted for level-1 to level-4.

2.4.6 Support Vector Machine Classification

The classification is done by conventional Support Vector Machine(SVM) algorithm using Gaussian radial basis function as kernel: $\exp(-\gamma * |u - v|^2)$. The dataset consists of 10 classes with 30 patterns in each class. Half of the dataset is used as training set and the other half is used as test set. SVM, matlab toolbox[20] have been used in this work for both classification and regression.

Class 1	$1.8 * 10^{-4}$
Class 2	$7.5 * 10^{-5}$
Class 3	$3.13 * 10^{-5}$
Class 4	$9.71 * 10^{-6}$
Class 5	$6.13 * 10^{-5}$
Class 6	$7.81 * 10^{-5}$
Class 7	$4.41 * 10^{-5}$
Class 8	$4.29 * 10^{-6}$
Class 9	$3.37 * 10^{-5}$
Class 10	$2.15 * 10^{-5}$

Table 2.1: C_n^2 values for each class

Feature Type	Level	Dimension	Success Rate %
DWT-Doubechies(N=4)	1	4	60
DWT-Doubechies(N=4)	3	10	76
DWT-biorthonal	1	4	66.67
DWT-biorthonal	3	10	75.33
Region Covariance	-	12	84.67
Region Covariance	-	25	82.67
Complex Wavelet Transform	1	12	90
Complex Wavelet Transform	2	24	83.33
Complex Wavelet Transform	3	36	86
Complex Wavelet Transform	4	48	88.67

Table 2.2: Success Rate and Feature Dimensions for each scenerio

Classes with their C_n^2 Labels given in Table 2.4.6. In Table 2.4.6, we can see that the success rates of the discrete wavelet transform for both doubechies and biorthonal filters are almost identical. Also they give us the least successful result. For the region covariance method, we can say that including the second order derivative does not improve our classification success, while the dimension increases. It is obvious from Table 2.4.6 that the complex wavelet transform gives us the best results in our trouts among our feature extraction methods.

2.4.7 SVM Regression

We have 10 classes each of them having 30 patterns. For each class, half of the randomly chosen paterns is used as a training data and the other half is used as a test data. Classes with its C_n^2 values are given in Table 2.1.

For SVM regression, conventional linear regression with e-insensitive loss function have been used. Kernel type which defines the type of mapping into a high dimensional feature space in SVM's is analyzed for each of the different features. The types of kernels are linear, polynomial, radial basis function and exponential radial basis function.

The proceeding figures are plotted by the following methodology. For each feature with its specific level of transform or specific level of derivatives, two plots have been done. The first one simply decides on a threshold value. Afterwards depending on the magnitude of the difference between the output and the real value, it is decided if the classification is done correctly or not. In the second one, the threshold is determined as the percentage of the actual C_n^2 parameter of each class.

All of the SVM Regression figures are plotted for the test data set.

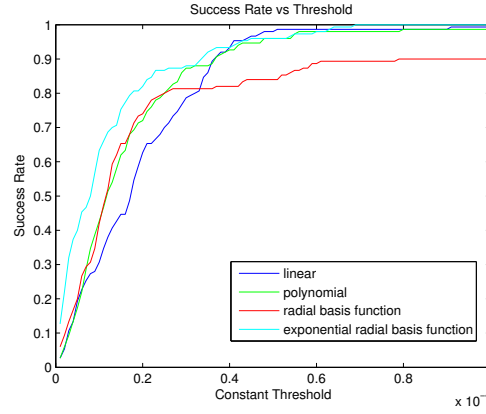


Figure 2.16: SVM Regression using 1-Level Wavelet transform with biorthogonal filter

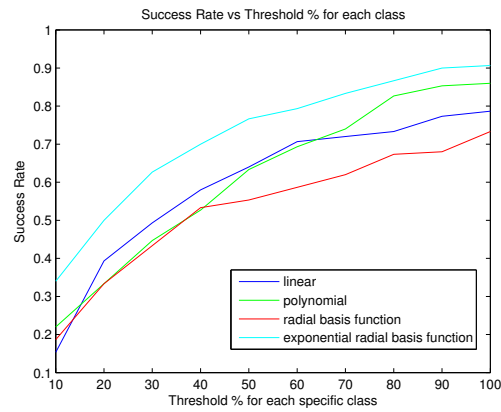


Figure 2.17: SVM Regression using 1-Level Wavelet transform with biorthogonal filter

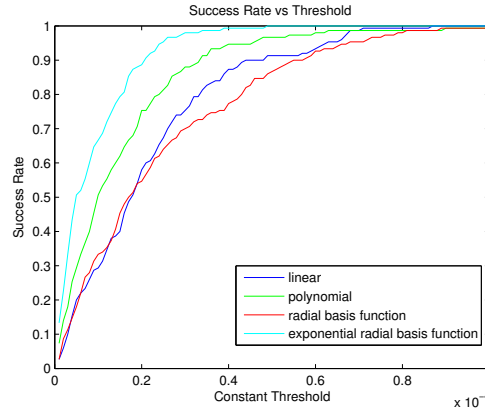


Figure 2.18: SVM Regression using 3-Level Wavelet transform with biorthogonal filter

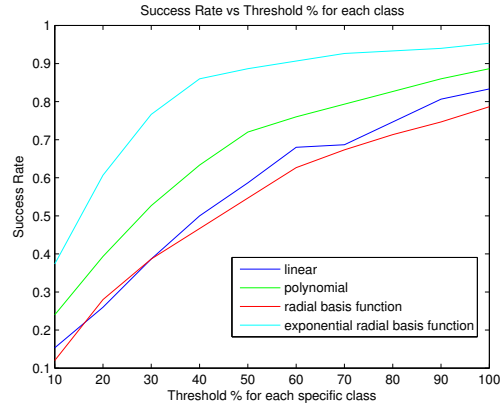


Figure 2.19: SVM Regression using 3-Level Wavelet transform with biorthogonal filter

It can be seen from Figures 2.16-2.19 that the feature dimension does not really differ in the sense of success rate. Only the SVM Regression with exponential radial basis function seems to work better as the dimension increases in our experiment. It can be seen from Figures 2.20-2.23 that as the feature dimension increases, the curse of dimensionality takes its place. It is also observed that the performance of each kernel functions are almost the same in 1-Level Wavelet Transform with doubechies filter.

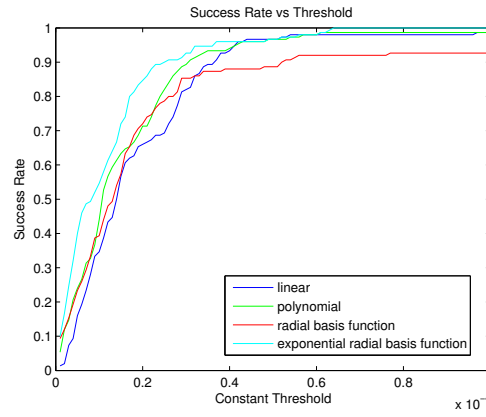


Figure 2.20: SVM Regression using 1-Level Wavelet transform with doubechies filter

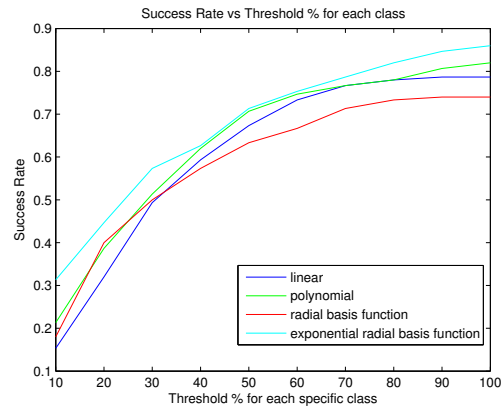


Figure 2.21: SVM Regression using 1-Level Wavelet transform with doubechies filter

It can be seen from Figures 2.24-2.27 that the region covariance matrix feature dimension after 12 have no effect in classification. The success rate in classification has no difference as the dimensions of the feature vector increases. It is most possible that the curse of dimensionality will occur as we increase the dimensions of the features.

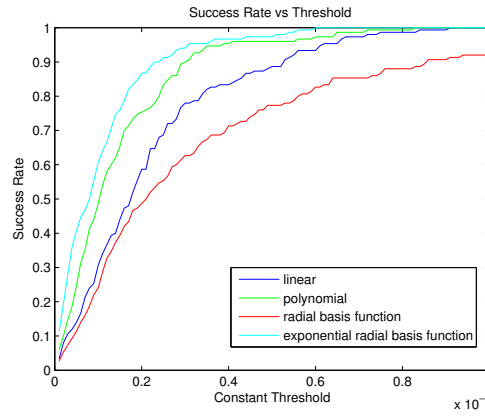


Figure 2.22: SVM Regression using 3-Level Wavelet transform with doubechies filter

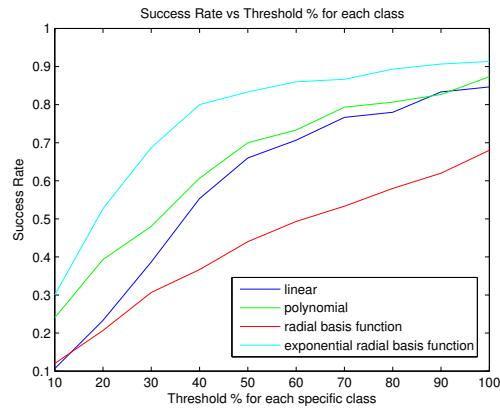


Figure 2.23: SVM Regression using 3-Level Wavelet transform with doubechies filter

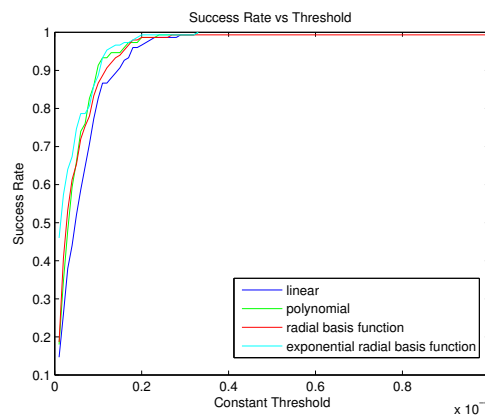


Figure 2.24: SVM Regression using Region Covariance method with first order statistics

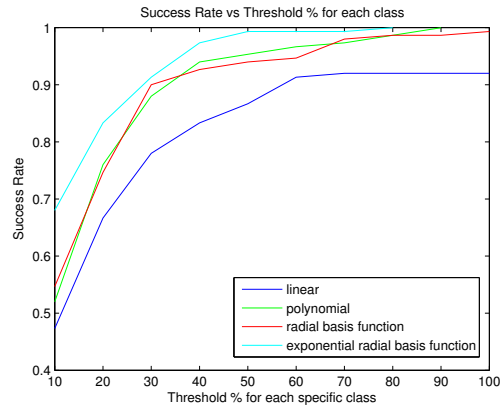


Figure 2.25: SVM Regression using Region Covariance method with first order statistics

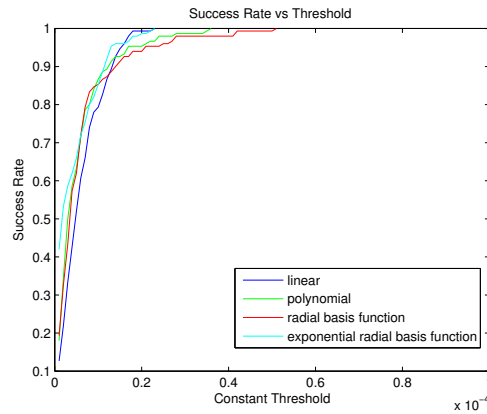


Figure 2.26: SVM Regression using Region Covariance method with second order statistics

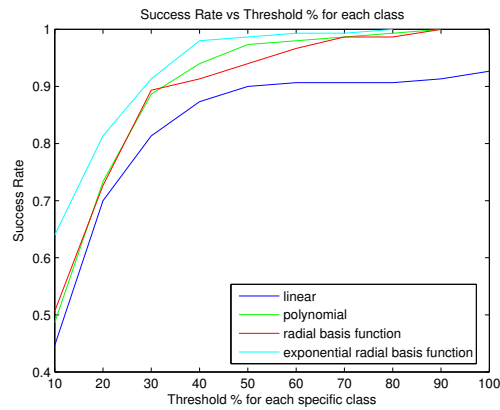


Figure 2.27: SVM Regression using Region Covariance method with second order statistics

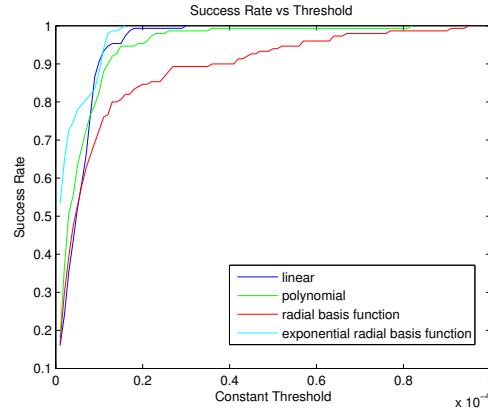


Figure 2.28: SVM Regression using 1-Level Complex Wavelet transform

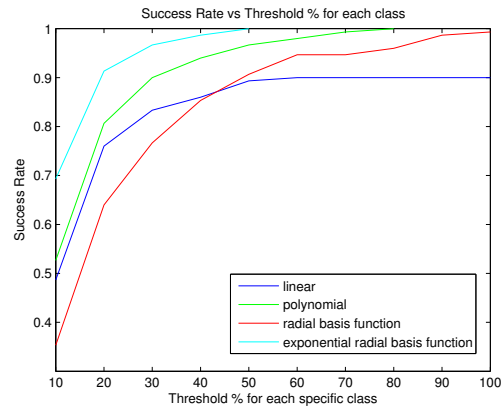


Figure 2.29: SVM Regression using 1-Level Complex Wavelet transform

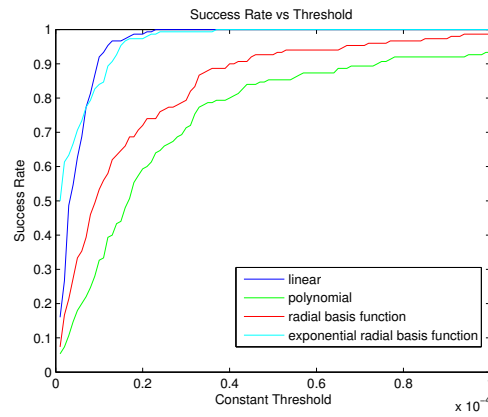


Figure 2.30: SVM Regression using 2-Level Complex Wavelet transform

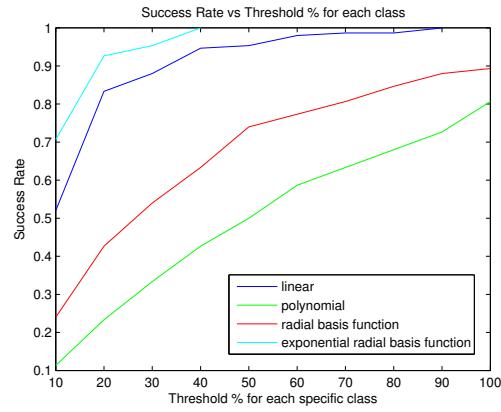


Figure 2.31: SVM Regression using 2-Level Complex Wavelet transform

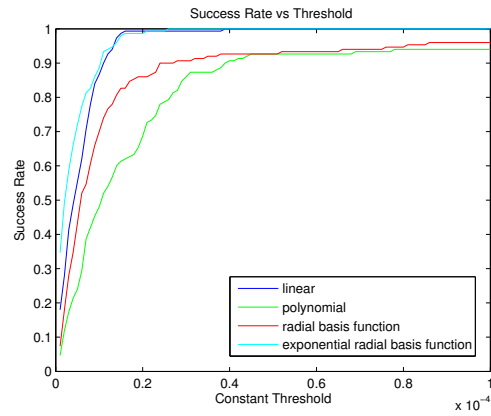


Figure 2.32: SVM Regression using 3-Level Complex Wavelet transform

Interesting complex wavelet transform effects can be seen from Figures 2.28 - 2.35. In 1-3 Level transforms, with a 10% threshold for each value we have above 70% success rate with the exponential radial basis function kernel.

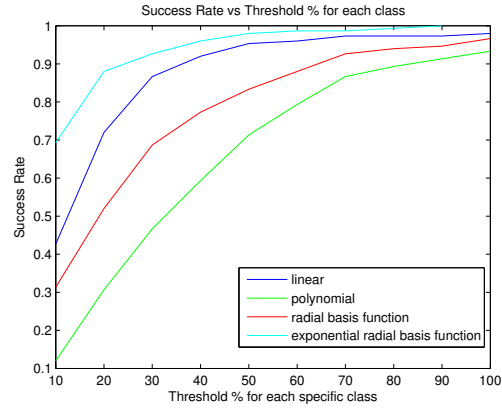


Figure 2.33: SVM Regression using 3-Level Complex Wavelet transform

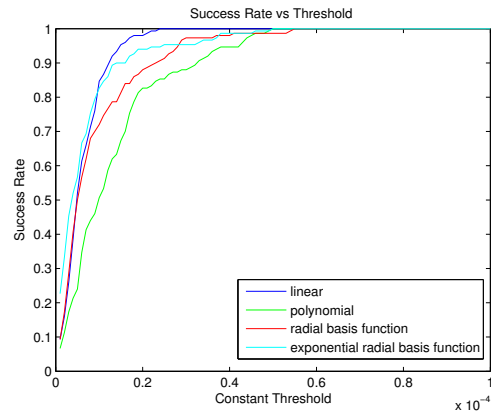


Figure 2.34: SVM Regression using 4-Level Complex Wavelet transform

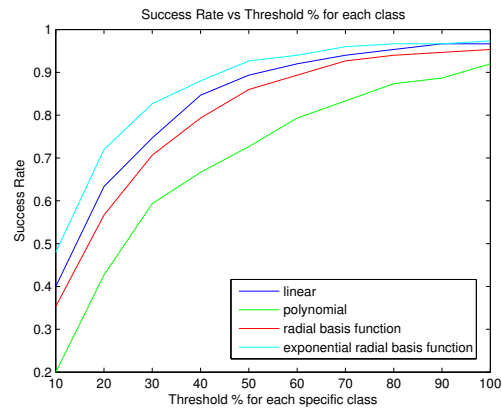


Figure 2.35: SVM Regression using 4-Level Complex Wavelet transform

2.4.8 Results and Conclusions

In this study, our main purpose was coming up with a regression method which will give us the strength of the turbulence. Since feature selection is one of the most important steps of the classification problem, we have tried three different methods which are Discrete Wavelet Transform, Complex Wavelet Transform and Region Covariance Method. As a result with the help of complex wavelet transform, we have 70% Success rate with 10% error margin and furthermore the success rate becomes above 90% with 20% error margin for each C_n^2 value of the classes that are weak to moderate-to-strong induced turbulence . This accomplishment can be used in real time FSO communication links to determine the strength of the turbulence instead of using expensive, time and power consuming bulky Scintillometers.

Chapter 3

Experimental Setup

3.1 Strong Turbulence Setup

3.1.1 Odeon Experimental Setup at Bilkent University

Existing empirical data within the weak and intermediate turbulence regimes using an 863 meters link about 1.2 meters above ground at the University of Maryland have been used to test our Aperture Averaging (AA) and image acquisition software and will be used in our model of turbulence. As it can be seen from Figure 3.1, using empirical data in intermediate turbulence conditions, the aperture averaging results demonstrate the expected reduction in intensity fluctuations with increasing aperture diameter.

The outdoor experimental setup has been completed and aligned ready for data collection at different weather conditions. The outdoor experimental location is chosen to be the Odeon Parking Lot at Bilkent University's Main Campus. The Length of the beam path is about 250 meters. The declination of the beam path is approximately 3.42° . The height of the transmitters and receivers is approximately one meter above the ground inducing strong turbulence to the

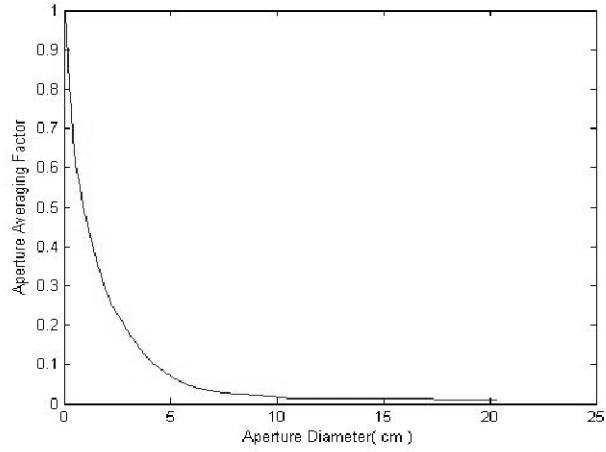


Figure 3.1: Aperture Averaging Factor For Intermediate turbulence conditions

propagating beam. Figure 3.2 shows a satellite picture of the experimental location chosen for the outdoor strong turbulence experiment. The transmitter part shown in Figures 3.3 and 3.4, setup on a portable breadboard with a rigid enclosure built specially to protect the equipment and optics from the rain and severe weather conditions. Since it is a flat, open area to be used for our outdoor link, we should be expecting strong winds and heavy rain for our setup. Our setup is strong and rigid enough to bear those winds and well enclosed for the water to leak. The enclosed transmitter setup is 15 kg excluding the heavy duty tripods. A rifle scope is placed at the top of the transmitter enclosure for the use in the alignment of the beam. The Electric power is supplied from Electric utility poles that exist in the experimental area.



Figure 3.2: Experimental Location

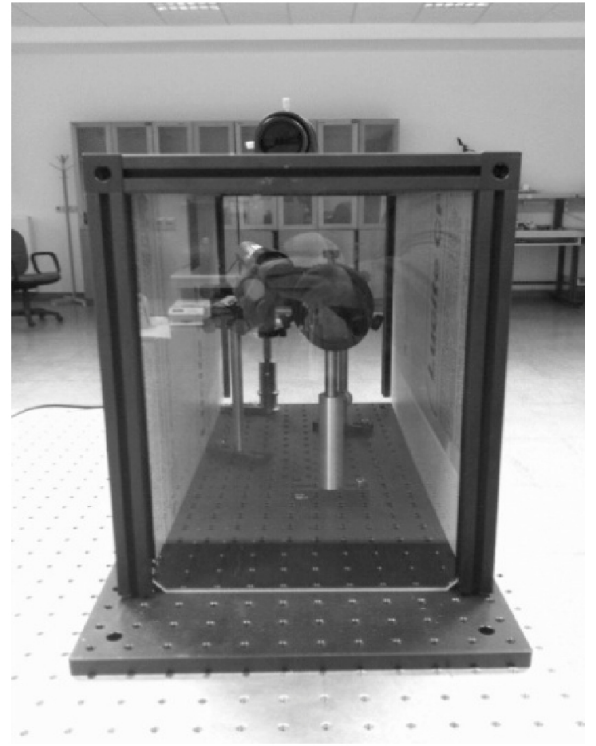


Figure 3.3: Enclosed Transmitter and Transmitter part front-view



Figure 3.4: Transmitter side with line-of-sight and Transmitter side (close view)

The receiver side consists of the Schmidt-Cassegrain telescope followed by the He-Ne filter and the CCD camera. The images are taken by a CCD camera which is connected to the frame-grabber card onto a laptop for capturing frames into AVI files. The receiver part (Figures 3.5, 3.6) is about 31.5 kg and is mounted on heavy duty tripods. An adapter has been especially constructed from aluminum for holding the He-Ne Filter to the telescope and the camera to the filter.



Figure 3.5: Receiver part - Front view and Receiver Part - Back view

With the help of the rifle scope, the alignment process has become an easy process. We used some white boards on the receiver side to center the beam onto the telescope. As the Gaussian beam travels over 250 meters, it expands in size and we center the beam at the receiver side to ensure the center part of the beam is seen by the telescope allowing us to use the plane-wave approximation in our calculations.

The sample images can be seen in Figure 3.7 . One side of the image is a little faded because of the difficulty we had with the settings of the camera. However



Figure 3.6: The receiver side showing line of sight. and Receiver side connected to CCD camera with an adapter

the aperture averaging and other statistical analysis are completely applicable within the more vivid part of the doughnut shape. Figure 3.8 shows us the Aperture Averaging Factor for the Bilkent University Strong Turbulence link. It can be seen that there is a strong decline within the 1 cm radius of the strong turbulent induced image. Then a saturation pattern is seen within the limits of the doughnut shape.

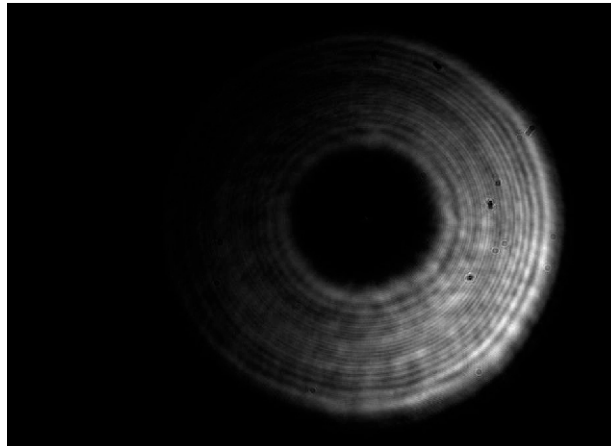


Figure 3.7: Sample images from Bilkent University Strong Turbulence Setup.

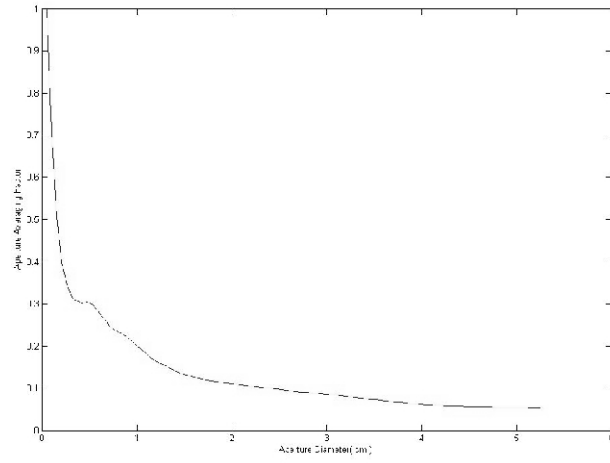


Figure 3.8: AA factor for the Bilkent University Strong Turbulence Setup.

3.1.2 Strong Turbulence Experiment at the University of Maryland

I have traveled to the University of Maryland at College Park (UMCP) the summer of 2011 to gather turbulence data using the Maryland Optics Group's (MOG) existing equipment. The overall schematic of the experiment can be seen in Figure 3.9.

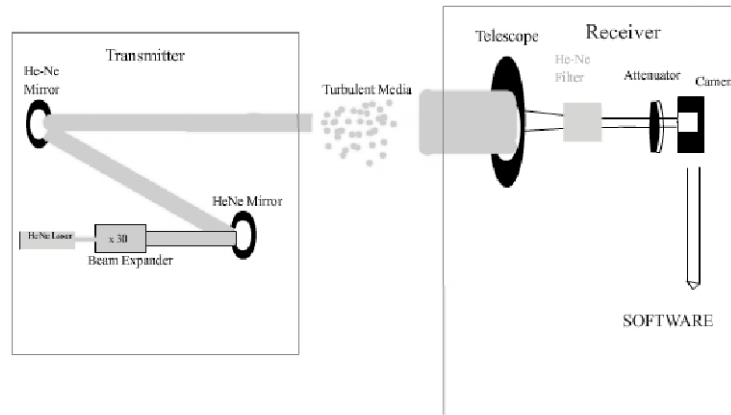


Figure 3.9: Overall Schematic of the experiment.

The experimental setup was assembled and taken outdoors to the Kim Engineering Building Parking Lot which represents a distance between the receiver and transmitter of about 120 meters. The selected site represents a uniform plain that is approximately 1.2 meters high above the ground to represent strong turbulence measurements.

The convenient line of sight chosen, as seen in Figure 3.10, has a green bush and a tree barrier on one side so it is suitable for creating big eddies along the way. The site is also close to power plugs at both ends of our experiment and the ground level is homogeneous from start to end which all play an important role on choosing our experimental location. A top view of the experiment is shown in Figure 3.11.



Figure 3.10: Line of Sight shown from the TX side.

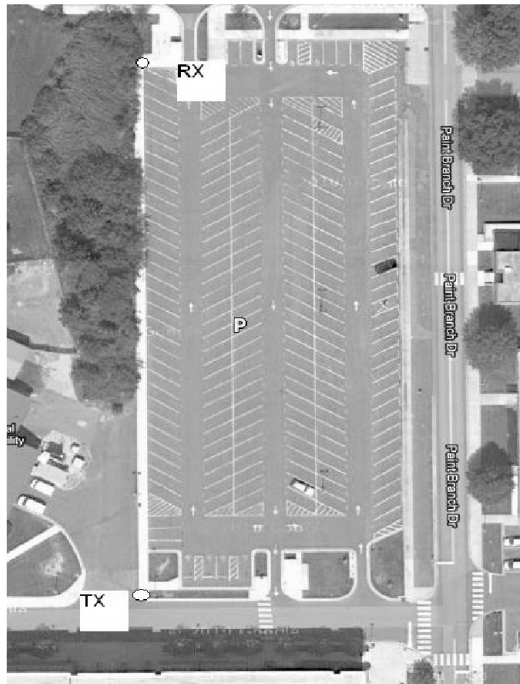


Figure 3.11: Top view of the experiment.

The transmitter and receiver side of the experiment can be seen in Figures 3.12 and 3.13. We have used a 35 mW laser with a 30x beam expander with a directional freedom we got with the special heavy-duty tripod in the transmitter side. In the receiver side, we have collected the beam with a Celestron telescope and stored the turbulence induced beam shape with the help of our focus adaptor and a CCD camera. We have used a Pulnix camera model TM1402-CL with 30 fps and 1392 x 1040 monochromatic resolution settings.



Figure 3.12: Transmitter Side.

The saturation at the CCD camera was critical. Depending on the humidity of the weather, we had to change the attenuation level of the beam that goes through the camera. For us to have a data that has most of the information that we are interested in, the dynamic range of the images' pixels must be well studied during the experiment and the attenuation should be chosen accordingly.



Figure 3.13: Receiver Side.

In case of choosing an attenuator that has big values and trying to increase the intensity of the image with the camera's built-in gain settings, it was observed to be an unsuccessful method. The intensity amplifier had just added an offset value through the doughnut shape and the turbulence effects are somehow averaged over spatial values and temporal values. Two moderate turbulence induced sequential images with high gain settings can be seen in Figure 3.14.

Before starting on storing the experimental data, images are taken as a sample and image processing techniques are applied in order to find where exactly the beam lies. Then, the histogram of the images is taken in order to compare the contrast of them. Low gain settings are applied in order to get rid of the amplifier noise in the image and the attenuator that results with the most dynamic contrast is chosen.

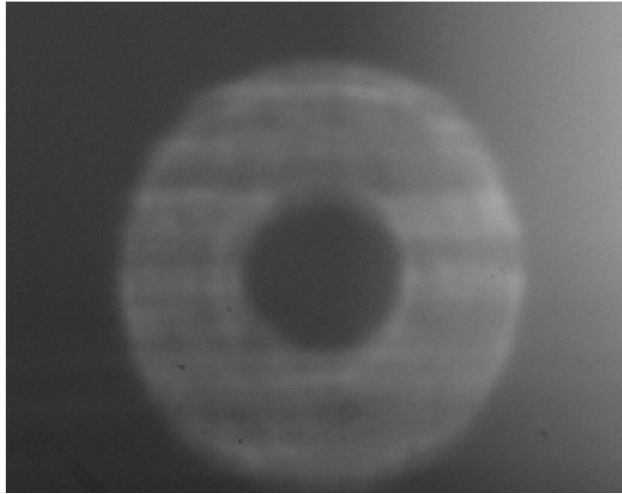


Figure 3.14: Faulty images with high gain settings.

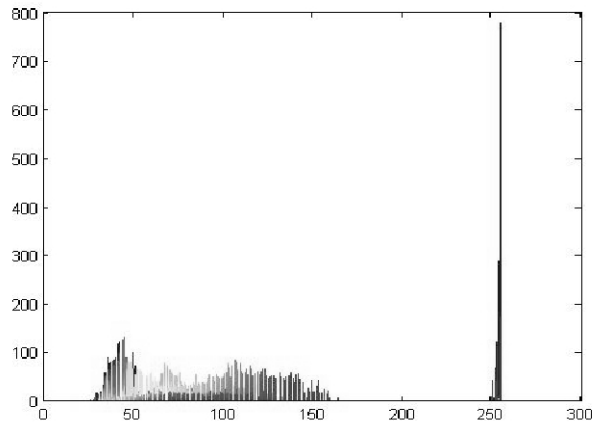


Figure 3.15: Histogram of Faulty images.

As we can see from Figure 3.15, the faulty image has interference with the background. The separation between the information and the noise seems to be interfering with each other. On the other hand when we look at the histogram of the appropriate image at Figure 3.16, the separation is much clearer. The transition from the noise (background) to information is almost flat.

Once proper attenuation settings are chosen and the appropriate images are located, image processing techniques using frame analysis are applied to find the aperture averaging factor. Such processing techniques applied to the images

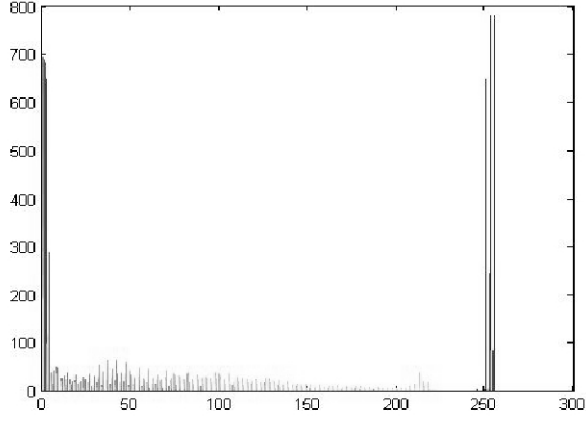


Figure 3.16: Histogram of Appropriate images.

have been discussed in detail in our article and will be skipped in this one[21]. A sample strong turbulence induced image can be seen in Figure 3.17.

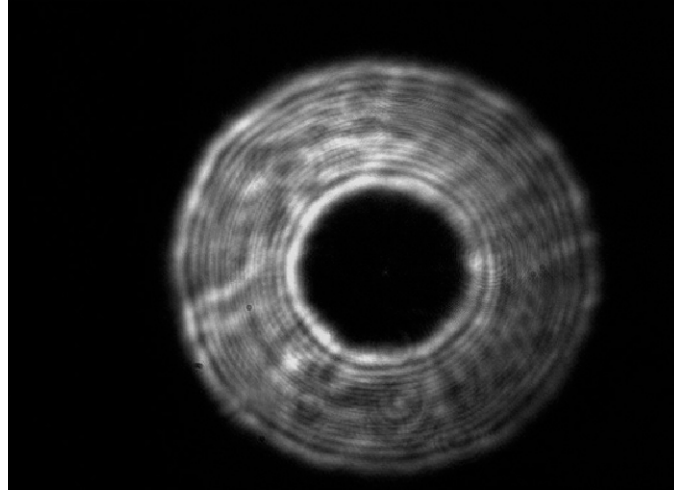


Figure 3.17: Sample of a strong turbulence induced beam shape

The main idea behind the AA Factor is given in Section 1.3. A frame analysis technique have been proposed and applied by Heba et. al [22]. Aperture averaging factor for different centers on the doughnut shape of the image can be seen in Figure 3.18. In some of the center points that are chosen, we weren't able to observe the expected decline on the Aperture Averaging (AA) curve. But as we increase the sequential turbulence induced images that we are analyzing, we are getting over this negative effect. The final characteristic point averaged Aperture

averaging factor that we have for strong turbulence data can be seen in Figure 3.19.

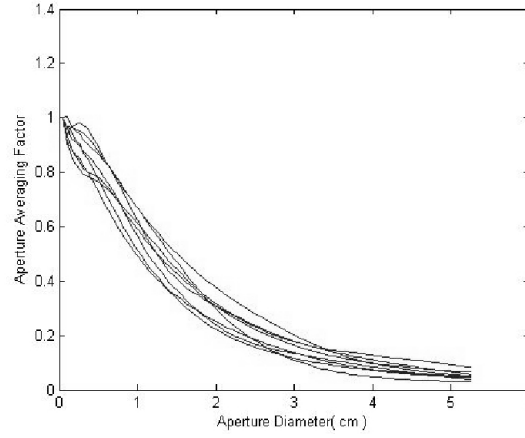


Figure 3.18: Aperture averaging factor for different center points on the beam.

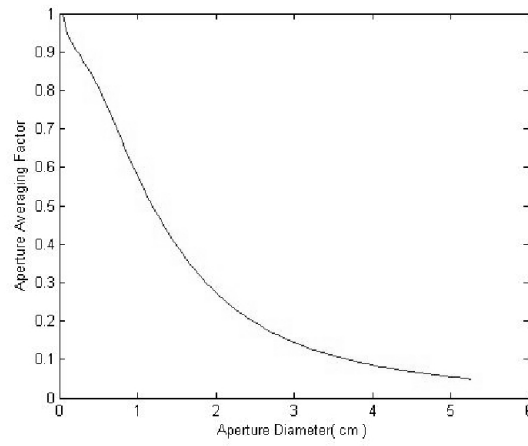


Figure 3.19: Point Averaged Aperture Averaging Factor for strong turbulence data.

The center points have been chosen randomly along the imaginary circle across the the frames between the inner radius and outer radius that are found in Section 2.3. An illustration for Point Averaged Aperture Averaging (PAAA) is shown in Figure 3.20.

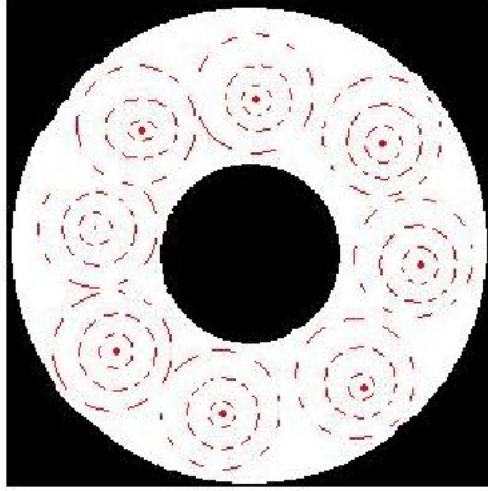


Figure 3.20: Illustration for Point Averaged Aperture Averaging

Especially in the saturation regime of the curve it gives excellent results in comparecent with the normal AA methods . The AA curve that is taken with in the same turbulence regime with 5 frames PAAA versus the 85 Frame with AA can be seen in Fig. 3.21. Using the spatial information from the large aperature telescope, we are able to create viable AA curves with computational ease.

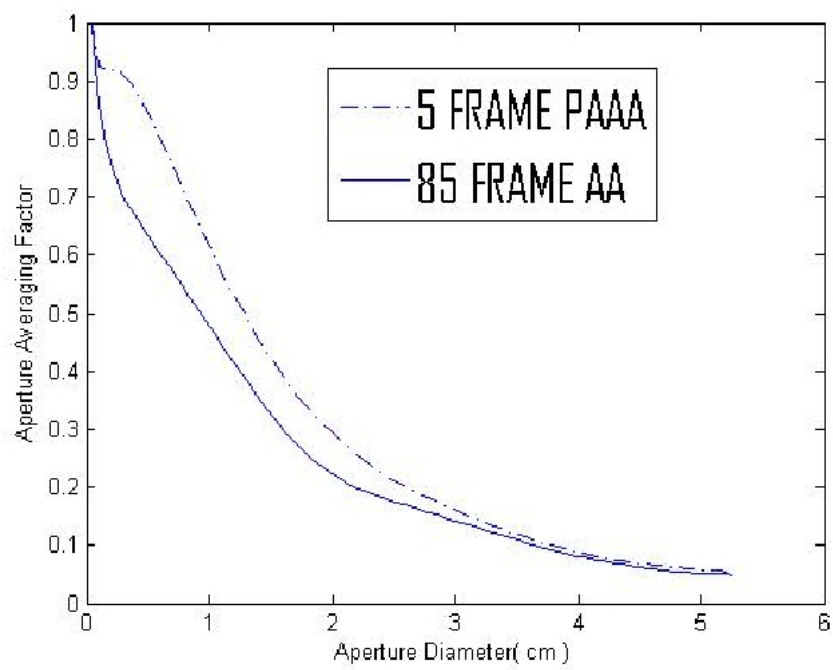


Figure 3.21: Point Averaged Aperture Averaging Factor for strong turbulence data.

3.2 Acquiring further weak & intermediate turbulence data using the University of Maryland Setup

We collected weak and intermediate turbulence data by taking our same experimental setup at the University of Maryland to a higher level above the ground. As Figure 3.22 shows, our transmitter was placed at the roof of the A.V. Williams Building and the Receiver has been setup at the rooftop of the Chesapeake Building. The Total Length of this line-of-sight Free-Space Optical (FSO) link is 952 meters and the whole experiment is about 12 meters above the ground.

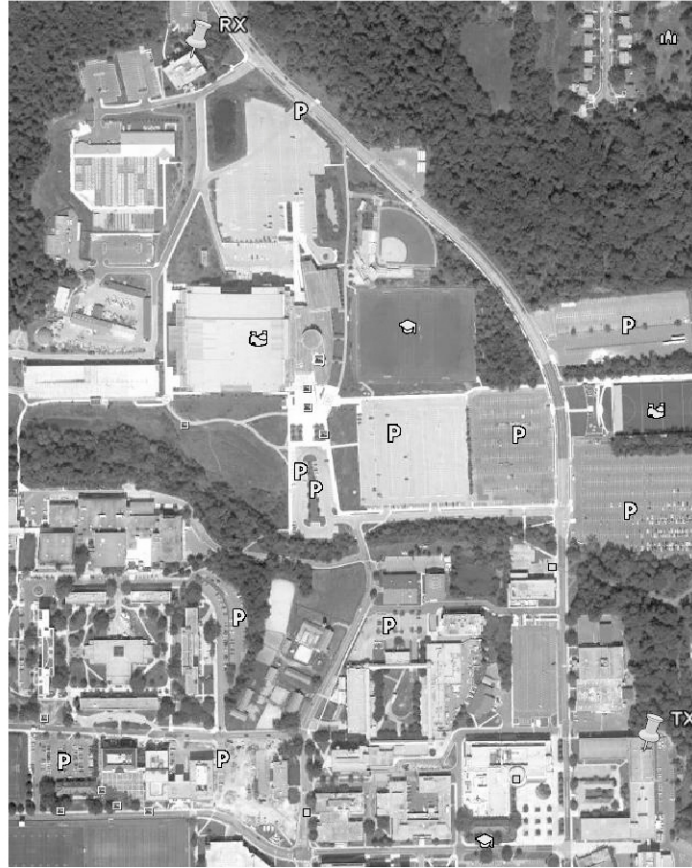


Figure 3.22: Weak-Intermediate Turbulence FSO Link.

The resultant beam shape from the weak-intermediate turbulence link is shown in Figure 3.23. There are a lot of stationary fringes on the images. It

is thought that these fringes were caused by the dirt on the optics. Although we cleaned all of the optic lenses, mirrors, front plane of the telescope, we weren't able to get rid of all of them. However, since they are stationary elements, they don't cause any trouble in our statistical operations.

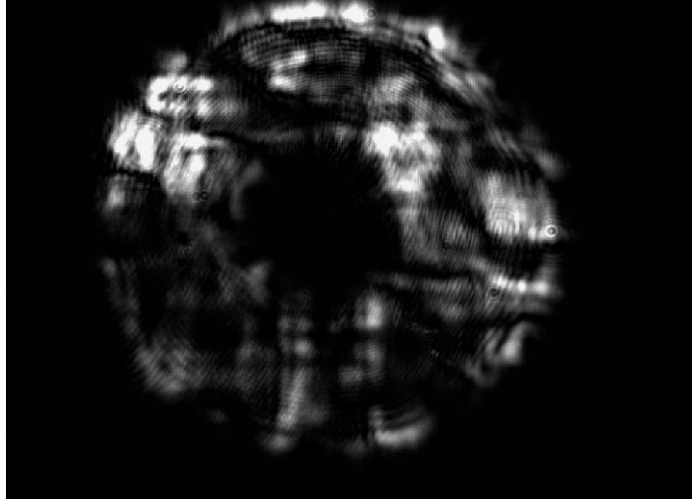


Figure 3.23: Weak Turbulence Beam Shape Results.

The Aperture Averaging Factor that is seen for this turbulence conditions has been plotted and is shown in Figure 3.24. The C_n^2 value of the atmospheric turbulence is 5.55×10^{-17} calculated using the Rytov variance equation. This shows us that we are in the weak turbulence regime. As we compare the Aperture Averaging Factors for different turbulent regimes as shown in Figures 3.19 and 3.24, we can see that there is a big difference in the slope of the curve. It seems that the stronger the turbulence, the steeper the initial decline in the curve and the faster the saturation at the tail of the curve. We can determine from this result that Aperture Averaging is more efficient for stronger turbulence. This can be valuable for us in the modeling of turbulence within the different turbulence regimes.

Weak turbulence theory is well explained and well studied in the literature. There are also some satisfactory explanations for the strong turbulence theory. But there is no well established study made for explaining all of the turbulence

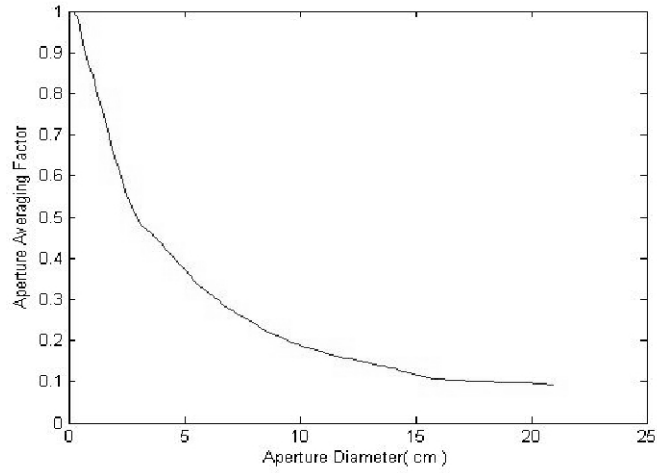


Figure 3.24: Aperture Averaging Factor For weak turbulence data.

regimes in one theory that is backed up by experimental data. In any kind of FSO system, to know the strength of the turbulence thus the C_n^2 value will be beneficial for us to determine the optimum bandwidth of the optimum communication link. Even if the FSO Link is placed 15 meters above the ground just to have weak turbulence effects, there can be severe atmospheric conditions that can change the turbulence regime.

If we would have a successful theory that will cover all regimes, we would have the chance of directly processing the image in existing or additional hardware thus deciding on the optimum bandwidth of the communication line rather than having a bandwidth check algorithm that will check its BER (Bit Error Rate) every period of time.

For this purpose, some turbulence strength estimation methods have been experimentally applied in order for us to study the effects of different parameters on the result. In section 3.3, different methods for calculating C_n^2 and hence the level of turbulence are introduced.

3.3 Analysis of the turbulence results in weak-to-strong turbulence regimes

In this section, we have presented weak and strong turbulence data using the University of Maryland setup as well as strong turbulence data using the Bilkent University setup. In addition, we have presented intermediate turbulence results from the University of Maryland setup in previous works [21]. Figure 3.26, is a combined curve for our results in the different turbulence regimes. In Figure 3.25, the weak turbulent measurements are taken in the low-rain and intermediate turbulent measurements are taken on a sunny day afternoon using the UMD Free Space optical link. Strong turbulent measurements are taken in the Bilkent University Strong Turbulent setup on a cloudless day. For each data, the Rytov variance Eq. 4.1 has been analyzed and then the data is labeled accordingly. We see the expected decrease in the AA curve in the weak turbulence regime. As the turbulence gets stronger, the decrease is sharper followed by a higher saturation.

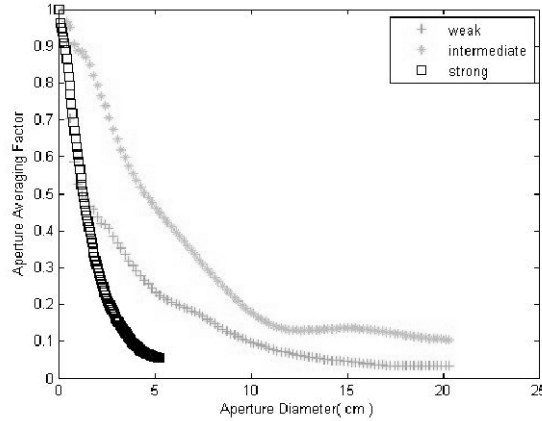


Figure 3.25: Combined Aperture Averaging Factors for different turbulence regimes.

In Figure 3.27, we are comparing the AA factor for our two strong turbulence experimental results. The height of the experiment is clearly a big factor in strong turbulence measurements. We have about 35 cm difference in terms of

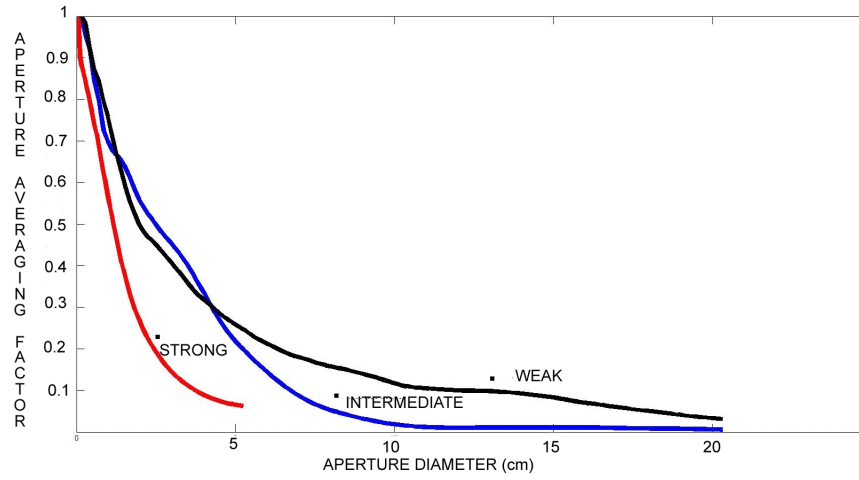


Figure 3.26: Combined AA Curves for different turbulence regimes.

height above the ground between the Bilkent University and the UMD setup which create some difference in the declination of the AA curves. Other reason for the difference could be realated to the varying weather conditions between the two setups like the humidity level, temperature, etc. Intensity variances are 108.4×10^{-6} in the Bilkent University Setup and 105.4×10^{-6} in the UMD Setup. Even though there is a little difference between them it is clearer from the Bilkent University results that we are getting stronger turbulence data than the University of Maryland setup.

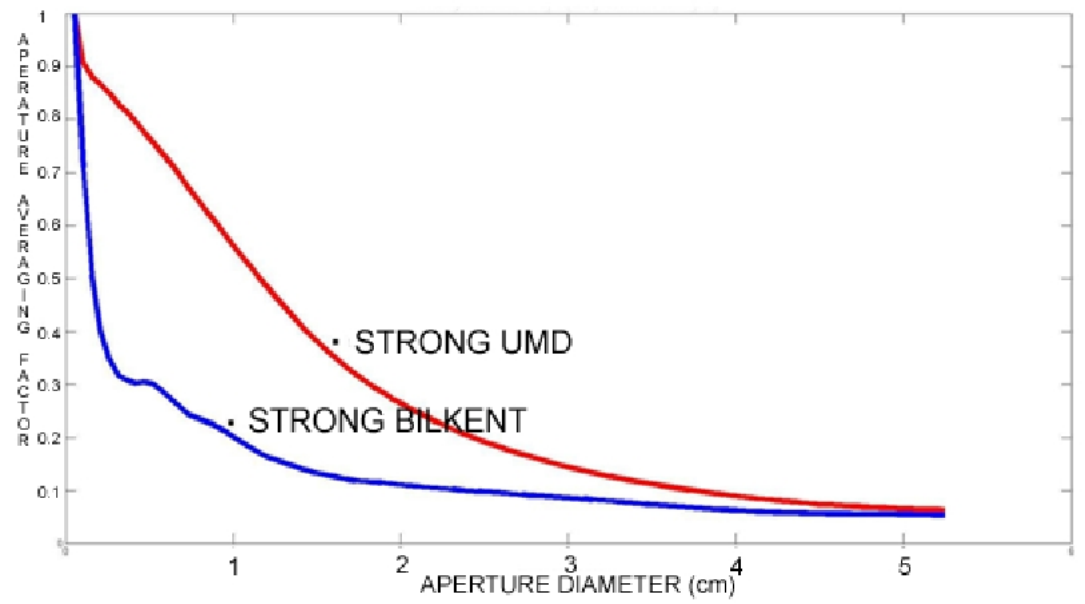


Figure 3.27: Bilkent University Strong Turbulence setup versus UMD Strong Turbulence Setup.

3.4 Proposed Methods for Estimating C_n^2 :

In the next subsections, two different methods for calculating C_n^2 , and hence the level of turbulence, are proposed. Such methods were preliminary investigated in this part and will be analyzed further within the next sections.

3.4.1 Portable C_n^2 Measurement using an Incoherent Source:

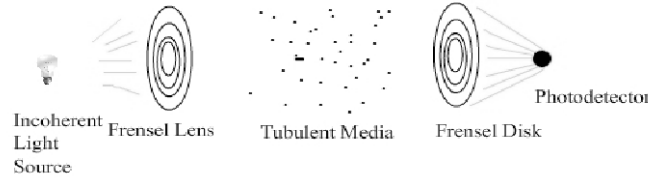


Figure 3.28: Portable C_n^2 Measurement Setup.

This experiment is done using "The Designers Edge Portable Power light" as an incoherent source as shown in Figure 3.28. A Photo detector (Thorlabs, PDA36A) has been chosen for its high gain capacities with small thermal and amplifier noise. The incoherent light source and photo detectors are placed right on the focus points of the Fresnel lenses. The first Fresnel Lens is used as a light guide and the second one is used for focusing the light on to the photo sensor. The downside of this setup is that since we cannot cover all of the sensory area of the photo detector, it needs to run a little bit more time in order to minimize any error that is caused by this effect.

A He-Ne filter has been used before the beam hits the photo detector in order for us to use the famous Rytov Approximation,

$$C_n^2 = \frac{\sigma_I^2}{1.23k^{7/6}L^{11/6}} \quad (3.1)$$

where the scintillation index is defined as,

$$\sigma_I^2 = \frac{\langle I^2 \rangle}{\langle I \rangle^2} - 1 \quad (3.2)$$

Unfortunately, the Rytov approximation is only valid for weak turbulence regimes. As the distance between the receiver and the transmitter gets smaller, we can get the read of strong turbulence regimes but as the C_n^2 value gets bigger as the distance gets really small so relying on the homogeneity of the turbulence strength along the path becomes really hard. So we have tried a compelling experiment by placing a howwave plate just infront of the laser in transmitter side. The C_n^2 values we have obtained for each minute in an hour is seen in Figure 3.29.

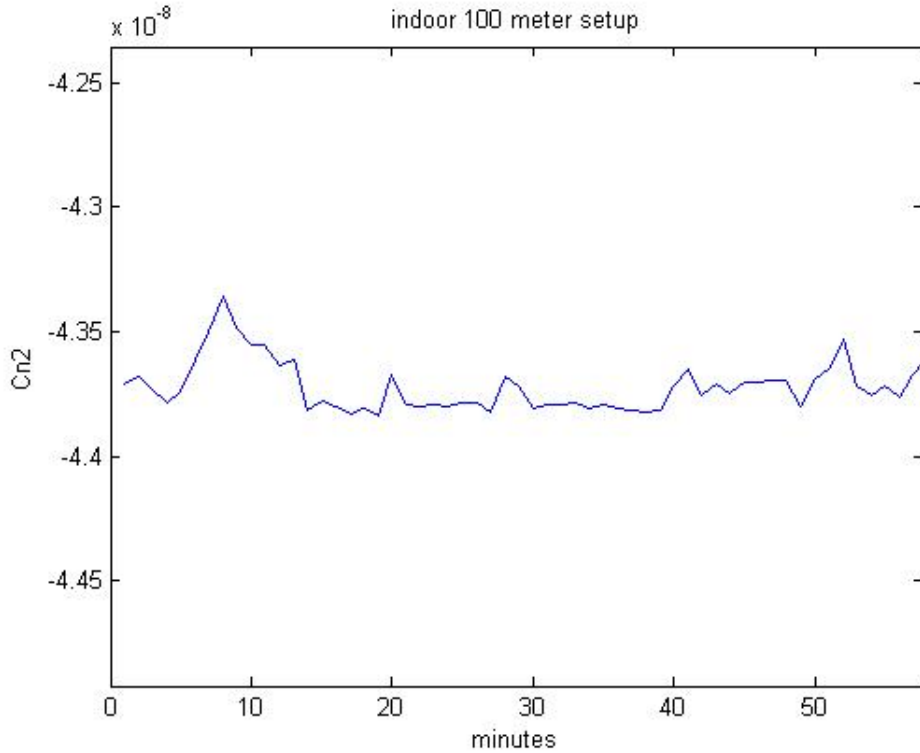


Figure 3.29: C_n^2 value in 100 meters- Hallway experiment with hotwave plate.

For the strong turbulence regime, the most accepted scintillation index model is defined by Andrews-Prokhorov for plane wave approximation as [3],

$$\sigma_I^2(L) = 1 + \frac{0.86}{(\sigma_R^2)^{2/5}}, \sigma_I^2 \gg 1 \quad (3.3)$$

Fortunately for us, as a result of our experiments in weak to strong turbulence regimes, it has been found that the AA factor is showing us some specific characteristics in different turbulence regimes. In very strong turbulence regimes, the most common characteristic is the fact that the AA factor does not diminish to small values as it does in weak turbulence conditions. Rather it stays up to some threshold and saturates in that value as it can be seen from Figure 3.26. We have tested using an incoherent light source within a floor hallway of a distance about 80 meters. In this new setup, we have changed the receiver side to be like the UMD receiver setup that we have used with the strong and weak turbulence measurements. This portable setup gave us accurate results for calculating C_n^2 within weak turbulence conditions showing that we don't need expensive or non-portable equipments like the Cassegrain telescope or the CCD camera for that purpose. Also, using an incoherent light source makes the alignment process much more feasible.

3.4.2 Turbulence Strength Estimation with Tracking Algorithm of the Beam from the Angle of Arrival (AOA) Variance

Design and testing of a turbulence monitor has been setup by NRL [23] where they have tried to estimate the C_n^2 value from the Angle of Arrival (AOA) fluctuations for different number of frames per seconds. The monitor gives us accurate results until moderate turbulence regimes (C_n^2 : 1×10^{-13}) in different conditioned beam paths.

Using geometrical optics and assuming a spherical wave (assuming light is a point source) with a small AOA, the relation between the C_n^2 and the radial AOA variance, σ_β^2 , is given by [2],

$$C_n^2 = \frac{\sigma_\beta^2 D^{1/3}}{1.093L} \quad (3.4)$$

where the $\sigma_\beta^2 = \sigma_X^2 + \sigma_Y^2$, D is the receiver aperture and L is the path length.

This method seems promising even for strong turbulence regimes. As long as the beam is inside the image we are taking we are going to be able to decide on the turbulence value. The mapping of the turbulence values in transition from weak to strong turbulence conditions will be decided according to the simultaneous measurements that will be taken. A weak turbulence link for weak-to-intermediate regimes is used for this purpose. The transmitter setup that is taken from the receiver side with a CCD camera is seen in Figure 3.30. In the transmitter setup, we have used an incoherent light source as in Section 3.4.1. The receiver side consists of a telescope followed by a CCD camera attached with an adapter. Modified version of the algorithm used for image acquisition to find the inner and outer radii has been applied to track the boundary of the beam in each segment.

As it can be seen in Figure 3.31, we are able to track the region where the changes and the corruptions that is caused by the turbulence induced to the beam. Using the same FSO link we have used for the weak-to-moderate turbulence experiments, C_n^2 values have been estimated throughout the day. The C_n^2 values we find are between 10^{-14} to 10^{-17} which are acceptable for the link we use.

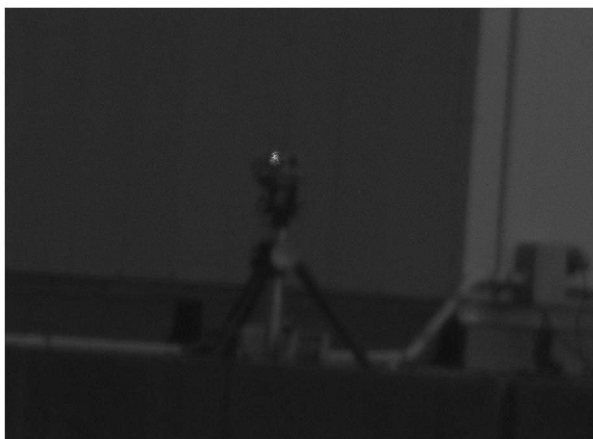


Figure 3.30: Overall picture of the transmitter with the beam to track on the middle.



Figure 3.31: Result of the Beam tracking Algorithm.

Chapter 4

Model of Turbulence in all of the Turbulence Regimes

4.1 Comparison of the strong turbulence data with theory

Scintillation is an inevitable phenomenon that occurs on any optical propagation system with a considerable distance. Tiny bit of temperature change along the optical path is all that is needed for fluctuations in the refractive index constant in the air. Intensity variations can be expressed as,

$$\sigma_I^2 = \frac{\langle I^2 \rangle}{\langle I \rangle^2} - 1 \quad (4.1)$$

where I is the Intensity at the receiving point detector.

The Rytov method provides a solution for the variance of the log intensity fluctuations seen by a point detector for a plane wave in weak turbulence conditions,

$$\sigma_I^2 = \langle (\ln I - \langle \ln I \rangle)^2 \rangle = 1.23 k^{7/6} L^{11/6} \quad (4.2)$$

Although the Rytov variance stands for weak turbulence fluctuations, in the literature it is considered a measure of turbulence strength by either increasing the refraction structure parameter (Cn^2) or the propagation path length (L) [24]. Behavior of the scintillation on the receiver point is somewhat interesting. Experimental and theoretical results showed that scintillation at the receiver increases with the Rytov variance until a maximum value. Then the weak nature of the turbulence decreases and strong turbulence inhomogeneities start to have a larger effect on the scintillation so by multiple scattering the scintillation slowly decreases and reaches to a saturation level [24].

In weak turbulence theory, it has been assumed that the correlation length of the intensity fluctuations is on the order of the first fresnel zone, $\sqrt{\frac{L}{k}}$, which is 9.8 mm for our weak turbulent experiments where the Length of the path is 951meters and $\lambda = 633nm$ and $\sqrt{\frac{L}{k}}$ is 3.5 mm for our 120 meters link at Bilkent University with the same λ . However in strong turbulence regimes the coherent beam becomes increasingly less coherent as it propagates and scintillation appears like the outcome of multiple sources with distinct but random phases [25].

4.2 The Andrews Asymptotic Analysis

The Andrews Asymptotic Analysis considers a plane wave with the assumption that the inner scale of turbulence is smaller than the spatial coherence radius of the plane optical wave p_0 where p_0 is defined by Fried as [26],[27],

$$p_0 = (1.46k^2LC_n^2)^{-3/5} \quad (4.3)$$

Using the Kolmogorov spectrum in the Andrews Asymptotic Analysis, the scintillation index in strong turbulence for the plane wave case is derived as [28],

$$\sigma_I^2(L) = 1 + \frac{0.86}{(\sigma_R^2)^{2/5}}, \sigma_I^2 \gg 1 \quad (4.4)$$

where σ_R^2 is the Rytov variance.

For the spherical wave case, the Andrews asymptotic analysis used the Kolmogorov spectrum to relate the irradiance variance in the saturation region to the plane wave Rytov variance [29],

$$\sigma_I^2(L) = 1 + \frac{2.73}{(\sigma_R^2)^{2/5}}, \sigma_I^2 \gg 1 \quad (4.5)$$

4.3 Churnside's Asymptotic Analysis

After the phenomenon of saturation of scintillation was understood, Churnside built upon Fried's work and published the first significant application of asymptotic theory to the study of aperture averaging. Churnside's result for the irradiance variance in strong turbulence for the plane wave case is,

$$\sigma_I^2(L) = 1 + \frac{1.14}{(\sigma_R^2)^{2/5}}, \sigma_I^2 \gg 1 \quad (4.6)$$

For the spherical wave case, the Churnside approximate of the scintillation index in strong turbulence is,

$$\sigma_I^2 = 1 + 3.86\left(\frac{kp_0^2}{L}\right)^{1/3}, \sigma_I^2 \gg 1 \quad (4.7)$$

where the coherence length for the spherical wave p_0 is,

$$p_0 = (0.546k^2 LC_n^2)^{-3/5} \quad (4.8)$$

The spherical wave scintillation index in strong turbulence can be expressed in terms of the plane wave Rytov variance as,

$$\sigma_I^2(L) = 1 + \frac{5.35}{(\sigma_R^2)^{2/5}}, \sigma_I^2 \gg 1 \quad (4.9)$$

4.4 Effective Kolmogorov Spectrum and Scintillation Index

Andrews and Phillips developed a model for the plane wave case that is valid under all fluctuation conditions. This was done through replacing the Kolmogorov spectrum with the effective Kolmogorov spectrum [30] [4] [31],

$$\Phi_{n,e}(K) = \Phi_n(K)|G_x(K) + G_y(K)| = 0.033C_n^2 K^{-11/3}[G_x(K) + G_y(K)] \quad (4.10)$$

where the large-scale filter function that passes only spatial frequencies $K < K_x$ is,

$$G_x(K) = \exp\left(-\frac{K^2}{K_x^2}\right) \quad (4.11)$$

and the small-scale filter function passing only $K > K_y$ is,

$$G_y(K) = \frac{K^{11/3}}{(K + K_y^2)^{11/6}} \quad (4.12)$$

Using the modified Rytov theory, the scintillation index is defined in terms of the large-scale σ_{lnx}^2 and small scale σ_{lny}^2 log irradiance fluctuations which are described in detail in Ref. [30],

$$\sigma_I^2 = \exp(\sigma_{lnx}^2 + \sigma_{lny}^2) - 1 \quad (4.13)$$

The scintillation index for a plane wave, excluding inner scale effects, is then defined to be [30], [4],

$$\sigma_I^2 = \exp\left(\frac{0.49\sigma_R^2}{(1 + 1.11\sigma_R^{12/5})^{7/6}} + \frac{0.51\sigma_R^2}{(1 + 1.69\sigma_R^{12/5})^{7/6}}\right) - 1 \quad (4.14)$$

where σ_R^2 is the Rytov variance for a plane wave. Eq. 4.14 reduces to the Rytov variance under weak turbulence conditions, and to the Andrews asymptotic model under strong turbulence conditions.

For a spherical wave, the scintillation index for zero inner scale effects is defined by [30], [4],

$$\sigma_I^2 = \exp\left(\frac{0.20\sigma_R^2}{(1 + 0.19\sigma_R^2)^{7/6}} + \frac{0.20\sigma_R^2}{(1 + 0.23\sigma_R^{12/5})^{5/6}}\right) - 1 \quad (4.15)$$

The main assumption is that the small-scale fluctuations are modulated by large-scale fluctuations of the wave. So the theory above treats the atmosphere like a linear spatial filter which causes the loss of transverse spatial coherence of the propagating wave by getting rid of scale sizes that are defined by the coherence radius and the scattering disk.

The heuristic approach based on the trusted physical arguments presented by Andrews et al. for Aperture Averaging Factor for moderate to strong turbulent

regimes is given below.

$$\sigma_{lnx,pl}^2(D, l_0) \cong 0.16\sigma_I^2\left(\frac{\hat{n}_x Q_1}{\hat{n}_x + Q_1}\right)^{7/6} [1 + 1.753\left(\frac{\hat{n}_x}{\hat{n}_x + Q_1}\right)^{1/2} - 0.252\left(\frac{\hat{n}_x}{\hat{n}_x + Q_1}\right)^{7/12}] \quad (4.16)$$

where, $Q_1 = LK_I^2/k = 10.89/kl_0^2$, $d = \sqrt{\frac{kD^2}{4L}}$ and $\sigma_I^2 = 1.23C_n^2 k^{7/6} L^{11/6}$ being the rytov variance.

$$\begin{aligned} \eta_x &= \frac{2.61}{1+0.45\sigma_I^2 Q_1^{1/6}}, \\ \hat{n}_x &= \frac{n_x}{1+\frac{d^2 n_x}{4}} = \frac{2.61}{1+0.623d^2+0.45\sigma_I^2 Q_1^{1/6}} \\ \hat{n}_x &= \frac{2.61}{1+0.623d^2+0.45\sigma_I^2 Q_1^{1/6}} \end{aligned} \quad (4.17)$$

So overall, the scintillation index parameter for moderate to strong turbulent regime with plane wave approximation is given,

$$\sigma_{l,pl}^2(D, l_0) = \exp[\sigma_{lnx,pl}^2(D, l_0) + \frac{0.51\sigma_I^2(1 + 0.69\sigma_I^2(1 + 0.69\sigma_I^{12/5}))^{-5/6}}{1 + 0.9d^2 + 0.621d^2\sigma_I^{12/5}}] - 1 \quad (4.18)$$

And the Aperture Averaging factor is defined by,

$$AAF = \frac{\sigma_{I,pl}(D)}{\sigma_{I,pl}(0)} \quad (4.19)$$

4.5 Comparison of the experimental data to the theory

Study of strong turbulence regimes have been very well investigated [21]. Theoretical results have been calculated for each central pixel point of the received beam. The general error margin is calculated by,

$$Error = \frac{1}{max_i} \sum_{i=1}^{max_i} ERR_i \quad (4.20)$$

where $ERR_i = 100 \frac{|Theo_i - Exp_i|}{Exp_i}$

In Figures 4.1-4.7, we compare the experimental results of the aperture averaging factors based on the theoretical model of Scintillation index model for varying C_n^2 , path length=120 m, inner scale, $l_0=5\text{mm}$ and wavelength $\lambda = 633 \times 10^{-9} \text{m}$.

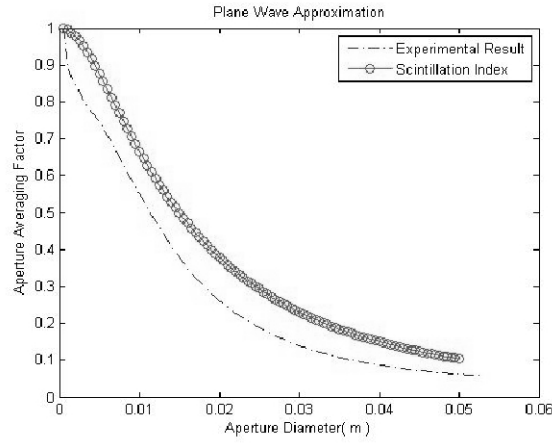


Figure 4.1: Experimental Results and Theoretical Results of Aperture Averaging Factor for C_n^2 structure parameter of 2.31×10^{-15} and Resulted Error margin of 36%.

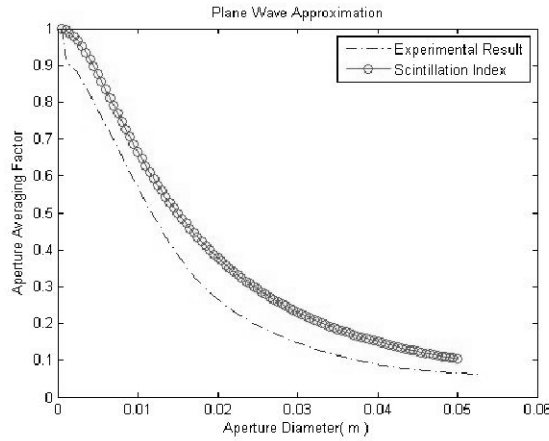


Figure 4.2: Experimental Results and Theoretical Results of Aperture Averaging Factor for C_n^2 structure parameter of 1.77×10^{-14} and Resulted Error margin of 32%.

As it can be seen from the analysis of the strongest segment of data on Figure 4.7, at a 5 cm aperture diameter there is a huge error on the convergence of the

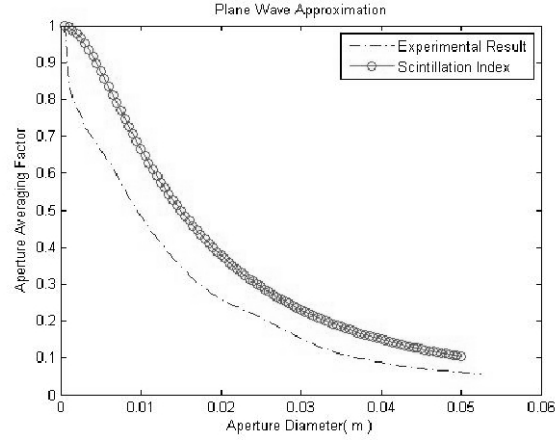


Figure 4.3: Experimental Results and Theoretical Results of Aperture Averaging Factor for Cn^2 structure parameter of 1.73×10^{-14} and Resulted Error margin of 44.76%.

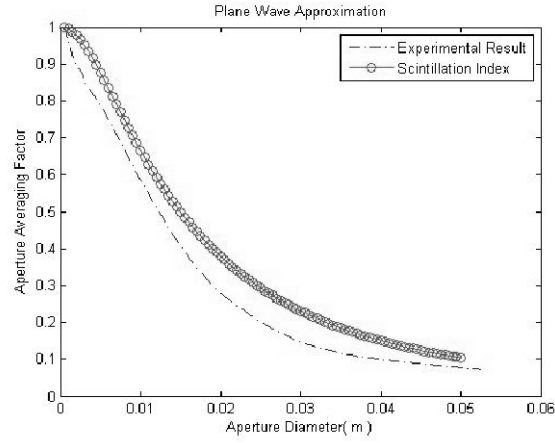


Figure 4.4: Experimental Results and Theoretical Results of Aperture Averaging Factor for Cn^2 structure parameter of 1.98×10^{-14} and Resulted Error margin of 27.5%.

Aperture Averaging curve. According to our founding's, as the Cn^2 increases prediction of the theoretical model stays below the experimental resulted curve but as Cn^2 decreases the resulted theoretical curve stays above the experimental result. For relatively weak turbulent regimes, the theoretical model gives us a pretty good match with the experimental data as can be seen in Figure 4.8. However we still should not be convinced with the results since for accurate Aperture Averaging Analysis the most important part is the Aperture Averaging

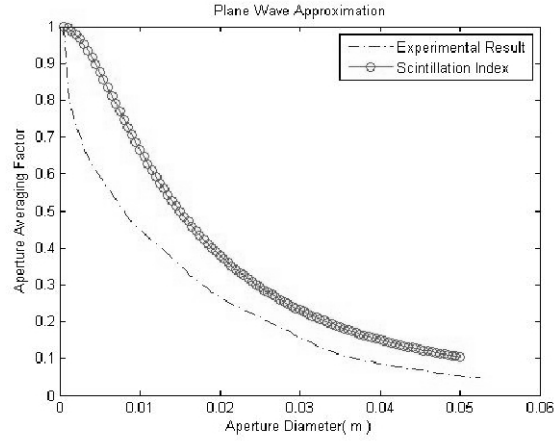


Figure 4.5: Experimental Results and Theoretical Results of Aperture Averaging Factor for Cn^2 structure parameter of 1.13×10^{-14} and Resulted Error margin of 50.69%.

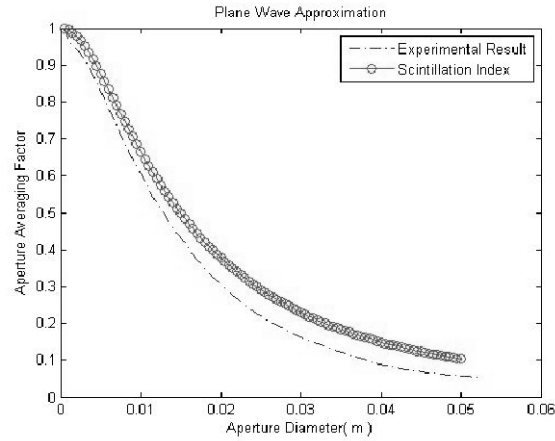


Figure 4.6: Experimental Results and Theoretical Results of Aperture Averaging Factor for Cn^2 structure parameter of 3.24×10^{-14} and Resulted Error margin of 22.97%.

factor for the biggest diameter or where the curve convergences and it still has a 50% error.

We can have a look at the overall picture modeling of the atmospheric turbulence in Figure 4.9. It is apparent that we have some downsides when it comes to strong turbulence regimes. As the AA Factor curve converges, scintillation index model is working fine with weak-to-moderate turbulent regimes but when the C_n^2 of the turbulent induced beam gets bigger the theoretical results stays very low

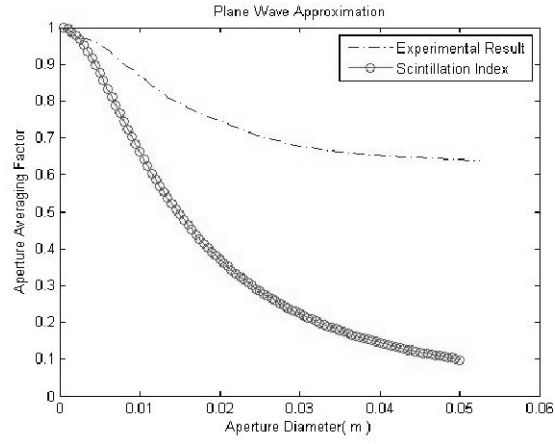


Figure 4.7: Experimental Results and Theoretical Results of Aperture Averaging Factor for Cn^2 structure parameter of 9.62×10^{-14} and Resulted Error margin of 50.69%.

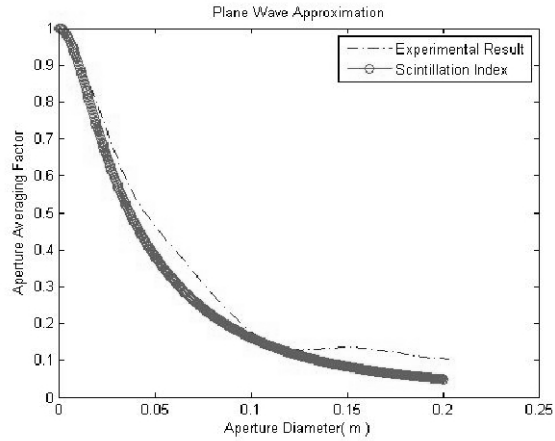


Figure 4.8: Experimental Results and Theoretical Results of Aperture Averaging Factor for Cn^2 structure parameter of 1.19×10^{-14} , link length of 951 m, and Resulted Error margin of 12.72%.

when you compare with the experimental results which makes the model useless practically as can be seen in Figure 4.7. The inner scale factor is an important parameter inside the scintillation index model and it is assumed 5mm throughout the analysis for strong turbulent regimes. Effects of the inner scale on intensity variances are investigated below.

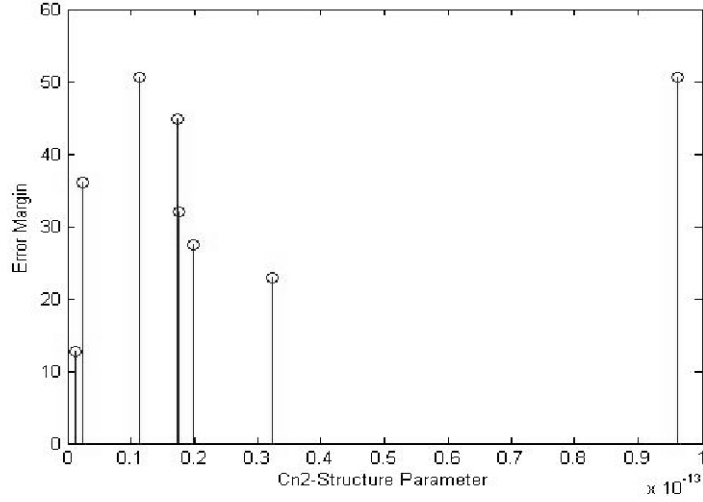


Figure 4.9: Error Margin for 5 cm diameter receiver vs. the C_n^2 structure parameter.

4.6 Effects of the inner scale

The energy in the atmosphere under the effect of the inertia break up into eddies and form a continuous pack of inner group starting from l_0 (inner scale of turbulence) to L_0 (outer scale of turbulence) with either velocity fluctuations or temperature fluctuations or both. The scale sizes that are smaller than inner scale l_0 , are assumed to be dissipated in the air as heat.

In terms of velocity fluctuations in the air which is appearing as wind, inner scale is defined by $l_0 = (v^3/\xi)^{1/4}$ where ξ is the energy dissipation rate and v is the viscosity. Outer scale, L_0 is proportional with the $\xi^{1/2}$; and generally assumed to be proportional with strength of the change in the path averaged mean flow velocity [32].

The general ideas of the velocity fluctuations also have been applied to the temperature fluctuations $\phi = T + \alpha_a h$ where ϕ is the potential temperature, α_a is the adiabatic rate of decrease in the temperature and h is the height above

the ground. So the inner scale is defined by $l_0 = 5.8(D^3/\xi)^{1/4}$ where D is the diffusivity of heat in the air (m^2/s) [32].

Near to the ground, inner scale of turbulence is typically between 1mm to 10 mm [32].

So the study of inner scale effects without a scintillometer is somewhat hard. In the work of Andrews et al. [32] inner scale have been measured between 1to10mm in strong turbulence regimes. In this work with scintillation index calculations, inner scale factor is assumed to be 5 mm. The effect of the inner scale factor can be seen in Figure 4.10. The error factors in strong turbulence analyses can very well be a cause of the effect of the difference of the real inner scale and the assumed. It is very clear from Figure 4.10 that even though there isn't much of a difference when the induced turbulence is weak, as the Rytov variance gets bigger, the effect of the inner scale becomes vital.

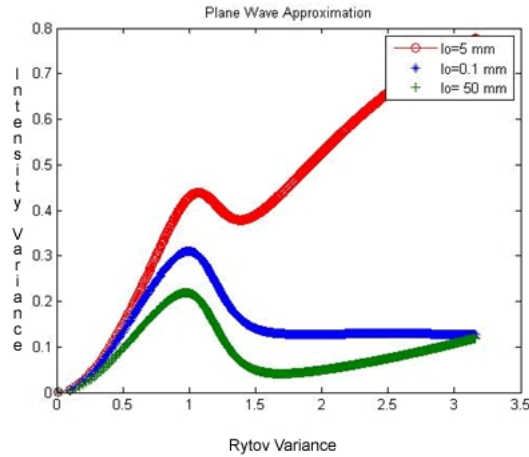


Figure 4.10: Intensity Variance vs. Rytov Variance for varying inner scale factors.

Effect of the receiving aperture is clearly seen in the Figure 4.11. With the right amount of receiver size it is clear that even though the Rytov variance

gets bigger the intensity variance can be optimized for optical communication regardless of the inner scale value.

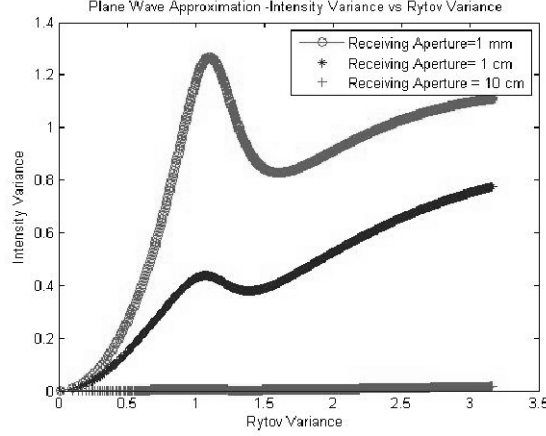


Figure 4.11: Intensity Variance vs. Rytov Variance for varying receiving aperture sizes.

4.7 Optimizing Receiver Design through analysis of the Aperture Averaging curves

In Figure 3.25, we see the combined aperture averaging factors of the weak, intermediate and strong turbulence regimes. Strong turbulence aperture averaging factor have reached saturation around 5 cm in aperture diameter which can be chosen as the optimum aperture size for this regime. It has a steep initial decline with a higher saturation. The data at intermediate turbulent regime has a lesser decline and is expected to reach small values of aperture averaging factor as the aperture diameter increases. The Aperture averaging factor for the intermediate turbulence curve seem to reach saturation at around 12cm which can be chosen as the optimum receiver size for this regime. The weak turbulence data has a similar decline until 2 cm of aperture diameter as the strong turbulence data but it changes dramatically after that point. After 16 cm of aperture diameter, there isn't a lot of change in the Aperture averaging factor so it can be chosen

as optimum aperture diameter for this specific weak turbulent regime. We can conclude from this result that the stronger the turbulence, the more effective the aperture averaging is in reducing the scintillation effects.

4.8 Optimizing System Performance through SNR and BER analysis

The performance of free space optical (FSO) links in a clear atmosphere is affected by the non-ideal characteristics of the communication channel. Atmospheric turbulence causes fluctuations in the received signal level, which increase the bit errors in a digital communication link. In order to quantify performance limitations, a better understanding of the effect of the intensity fluctuations on the received signal at all turbulence levels is needed. For this reason, in this section, optimizing system performance will be analyzed by calculating the Signal-to-noise ratio and the BER for the data taken in the Bilkent Odeon setup. First, the theoretical equations for these parameters will be demonstrated below.

It is found experimentally that for both weak turbulence $\sigma_{\ln I_R}^2 < 0.3$, and strong turbulence $25 < \sigma_{\ln I_R}^2 < 100$ the distribution of log field amplitude is a normal distribution, as are the log intensity variations measured at a point [33]. The probability distribution for normalized intensity is given by [28],

$$p(i) = \frac{1}{(2\pi\sigma_I^2)^{1/2}} \frac{1}{i} \exp\left[-\frac{1}{2\sigma_I^2}(\ln i + \frac{1}{2}\sigma_I^2)^2\right] \quad (4.21)$$

In the absence of turbulence, the received detector signal corresponding to a “one” has a steady value $\langle I \rangle$, and the normalized received signal is 1. In this case the BER can be calculated by assuming the errors result from receiver noise, which is assumed to be Gaussian distributed about zero. For a detector whose

noise is Gaussian distributed about zero with a variance $\langle i_N^2 \rangle$ the probability that the noise is below a set level i_s is

$$p(i_N \leq i_s) = \frac{1}{\sigma\sqrt{2\pi}} \int_{-\infty}^{i_s} e^{-x^2/2\sigma^2} dx \quad (4.22)$$

where $\sigma^2 = \langle i_N^2 \rangle$. The signal-to-noise (S/N) ratio is

$$\frac{S}{N} = \frac{\langle I \rangle^2}{\sigma^2} \quad (4.23)$$

In on-off keyed (OOK) systems, the probability distributions of either noise alone or signal plus noise is assumed to be Gaussian. Thus, if the threshold level is set at half the average signal level, the overall probability of error is

$$BER = \frac{1}{2}(p_{one} + p_{zero}) = \frac{1}{2}[p(i_N < -I/2) + p(i_N > I/2)] = \frac{1}{2}erfc\left(\frac{1}{2\sqrt{2}}\sqrt{\frac{S}{N}}\right) \quad (4.24)$$

In the presence of optical turbulence, the probability of error in Eq. 4.4 must be averaged over the intensity fluctuation corresponding to a received “one”. In this case, at any instant the actual received S/N ratio will rise or fall depending on whether the turbulence causes a “fade” or a “surge”. The probability of a “zero” error, which is equivalent to the BER in the absence of turbulence, does not change because there is no received signal when a “zero” arrives and can be written as [28],

$$p_{zero} = \frac{1}{2}erfc\left(\frac{1}{2\sqrt{2}}\sqrt{\frac{S}{N}}\right) \quad (4.25)$$

However, the probability of a “one” error is now

$$p_{one} = \frac{1}{2}erfc\left((i - 1/2)\frac{1}{\sqrt{2}}\sqrt{\frac{S}{N}}\right) \quad (4.26)$$

where i is the detector signal corresponding to the actual received normalized intensity.

To compute the average BER, the product of the probability of a “one” error and the probability distribution for the normalized intensity (Eq. 4.1) must be integrated over all possible intensity values [28],

$$\langle p_{one} \rangle = \int_0^\infty \frac{1}{2} \text{erfc}(i - 1/2) \frac{1}{\sqrt{2}} \sqrt{\frac{S}{N}} \frac{1}{(2\pi\sigma_I^2)^{1/2}} \frac{1}{i} \exp\left(\frac{-1}{2\sigma_I^2}(\ln i + \frac{1}{2}\sigma_I^2)^2\right) di \quad (4.27)$$

which gives,

$$\langle BER \rangle = \frac{1}{2}(\langle p_{one} \rangle + p_{zero}) \quad (4.28)$$

From each of the turbulent induced “.avi” file, 3 seconds of segments have been saved along with their calculated C_n^2 results according to Eq. 4.12. The variations on the refractive index structure can clearly be seen in Figure 4.12. In this example we have a maximum of C_n^2 of 9.61×10^{-14} and minimum of 6.57×10^{-15} . C_n^2 variance in this example is 4.6810^{-028} .

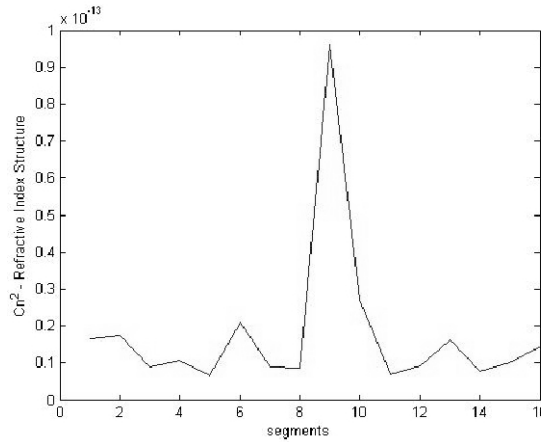


Figure 4.12: 3 sec. segments and C_n^2 behavior in time.

Signal to Noise Ratio and Bit-Error-Rates are clearly effective parameters when it comes to analyzing the effects of the strength of the turbulence in wireless optical communication link. In our turbulence setup, the configuration of the CCD camera was taken with a 30 ms shutter speed with 30 fps. Then as a result of the frame analysis technique that we have proposed in the previous sections for finding where the beam lies, there have been 8 equidistant points chosen for finding out the point averaged aperture averaging values as the center of the preassumed receiver lenses. According to the acquisition of the boundary of the doughnut shape, which is changing literally in every other frame, maximum aperture size(R_{max}) is chosen for the analysis. Finally taking the 8-equidistant points as a reference the pixel locations for the receiving apertures in terms of nearness to the center pixel have been stored in a sense of decreasing the computational complexity. Eq. 4.23) have been applied for the ‘1’bit and ‘0’bit cases.

Other than using a controllable shutter in front of the laser within the transmitter setup, we have taken the background images when the laser is off and turned on the laser manually inside the same measurement within a short time period. Assuming that the turbulent media is not erratic within this time frame, which is reasonable when we analyze Figure 4.12, BER can be calculated according to Eq. (31) and SNR ratio is calculated according to Eq. 4.23).

To investigate the change in the strength of the turbulence in a short time period, the aperture averaging factor has been calculated for 1 second of segments for total of 6 seconds in Figure 4.13. The data that is chosen is taken from strong turbulence setup for the sake of having inhomogeneous property in our measurement. Variance of the aperture averaging factor at a 5 cm receiving aperture is found to be 9.6310–006.

So for low bandwidths of wireless communication links, our way of measuring the SNR and BER seems reasonable. As a result, for a 5 cm receiving aperture

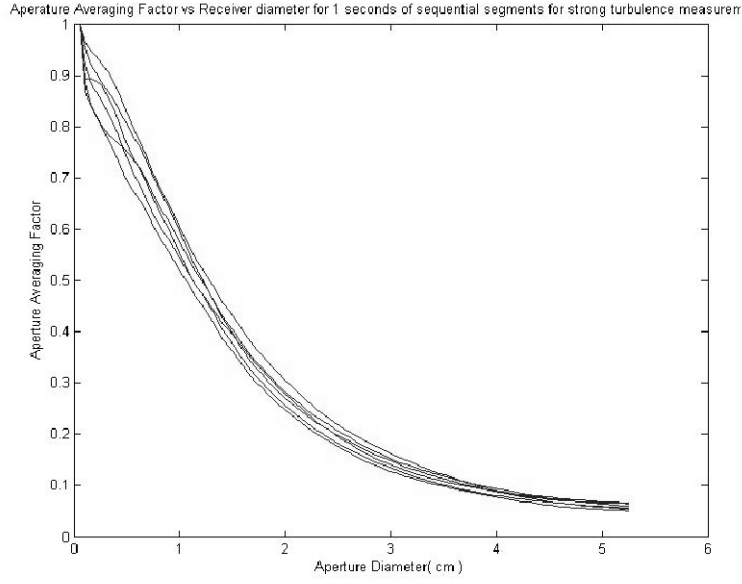


Figure 4.13: Aperture Averaging Factor vs Receiver diameter for 1 seconds of sequential segments for strong turbulence measurements.

our way of calculation of SNR and BER should give out comparable results for optimum receiver design between different turbulent regimes. The resulted Bit Error Rate and Signal-to-Noise Ratios are given in Figures 4.14- 4.19 for different turbulent regimes. In Figure 4.14 we can see that for relatively weaker turbulent conditions $C_n^2 = 6.57 \times 10^{-15}$, 1 cm of aperture diameter is all that is needed for the optimum size receiver. But as it is seen in Figure 4.16 for turbulence strength of $C_n^2 = 3.24 \times 10^{-14}$ saturation hasn't been established in 5 cm. Bigger diameter of aperture sizes is needed for the analysis of the optimum receiver. In Figure 4.18 where the $C_n^2 = 9.59 \times 10^{-14}$, saturation is established in 4 cm of diameter size but the SNR value is really low when you compare it to the weaker turbulent regime.

As it can be seen from Figure 4.20, the SNR ratio at 5 cm diameter aperture is clearly increasing as the C_n^2 decreases. The data that is used in this graph is from the same experiment side so the total length of the propagation is the same. Due to the characteristics of Intensity variations vs. Rytov Variance, saturation in the SNR value is expected as the C_n^2 increases.

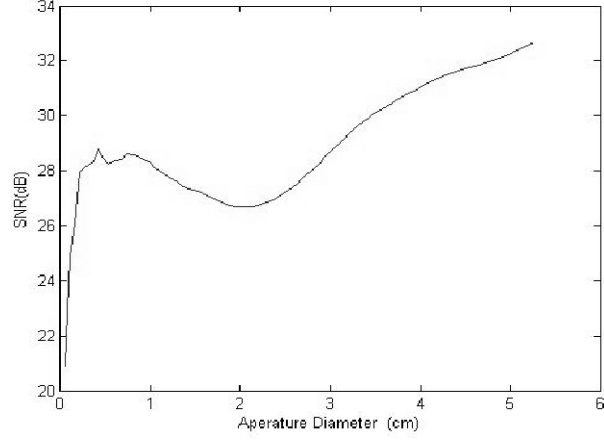


Figure 4.14: SNR rate for strong turbulence measurements in UMD setup for different Aperture diameters at the receiver where $C_n^2 = 6.57 \times 10^{-15}$.

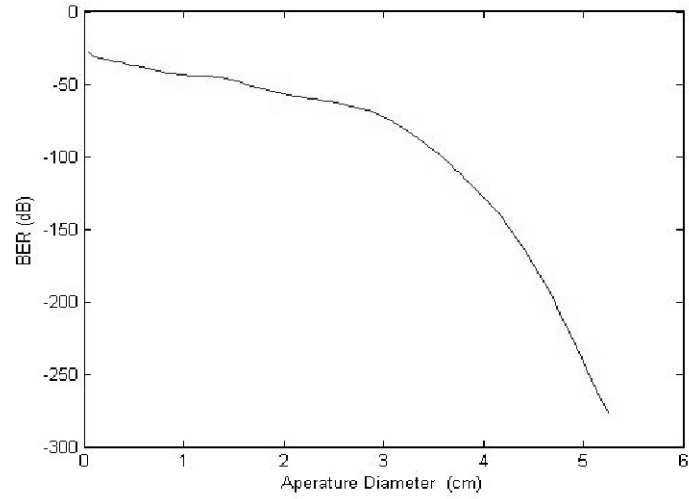


Figure 4.15: BER rate for strong turbulence measurements in UMD setup for different Aperture diameters at the receiver where $C_n^2 = 6.57 \times 10^{-15}$.

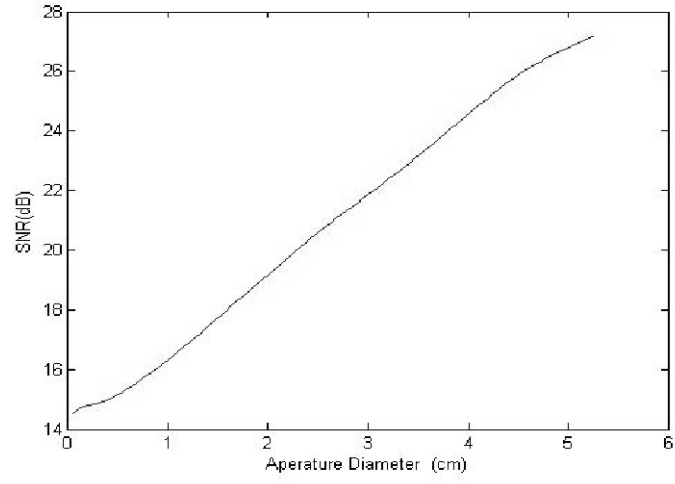


Figure 4.16: SNR rate for strong turbulence measurements in UMD setup for different Aperture diameters at the receiver where $C_n^2 = 3.24 \times 10^{-14}$.

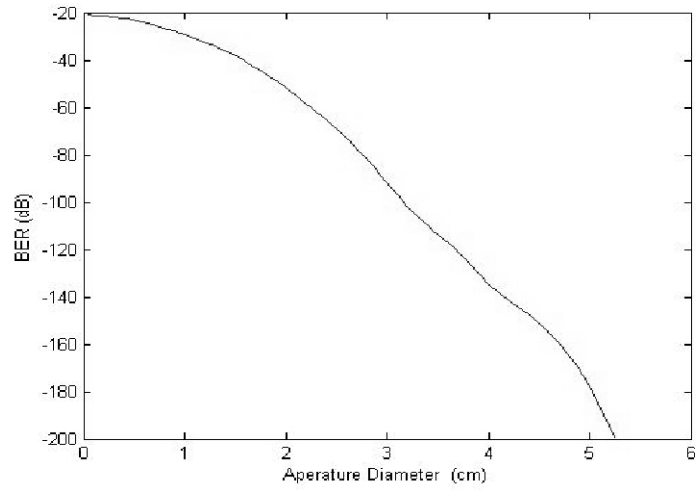


Figure 4.17: BER rate for strong turbulence measurements in UMD setup for different Aperture diameters at the receiver where $C_n^2 = 3.24 \times 10^{-14}$.

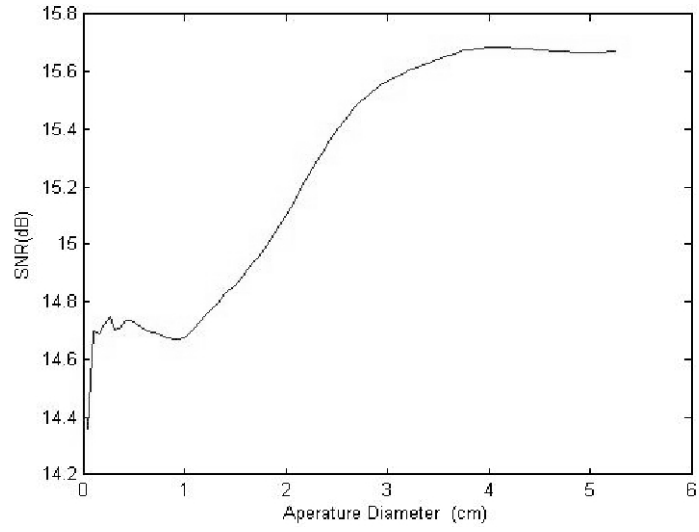


Figure 4.18: SNR rate for strong turbulence measurements in UMD setup for different Aperture diameters at the receiver where $C_n^2 = 9.59 \times 10^{-14}$.

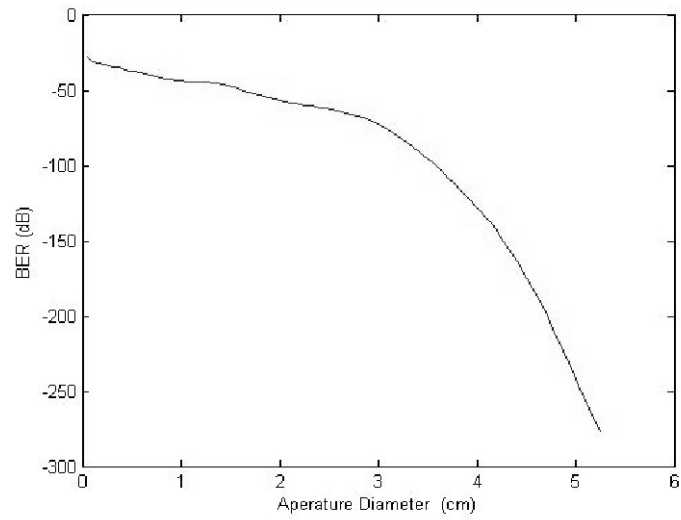


Figure 4.19: BER rate for strong turbulence measurements in UMD setup for different Aperture diameters at the receiver where $C_n^2 = 9.59 \times 10^{-14}$.

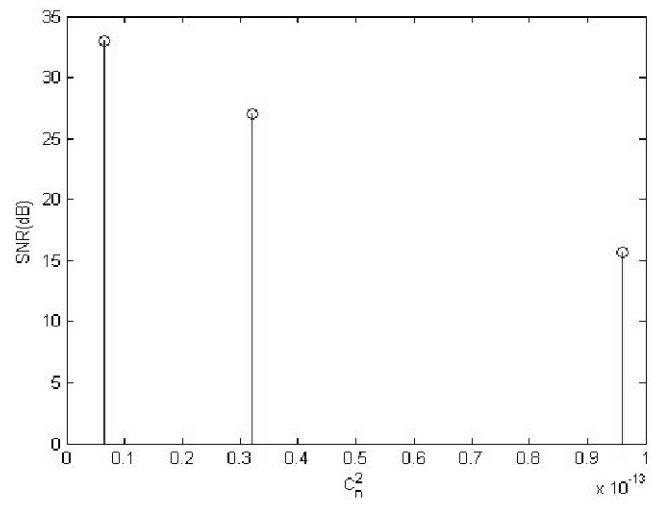


Figure 4.20: SNR vs. C_n^2 .

Chapter 5

Conclusion

In this thesis, a strong turbulence experimental setup for investigating the effects of AA Factor in FSO communication system is proposed. PAAA is proposed for analysis of AA Factors in strong turbulence regimes with less computational complexity. With the help of our strong turbulence experimental setup we have tested the Scintillation Index model which is the most accepted model in literature. It has been found that there is a good correlation between the Scintillation Index model and our experimental data for the AA factor when it comes to weak-to-intermediate turbulence regimes. However, for the strong turbulence regime, the model seems not to match the AA factor results from our experimental turbulence data. In addition, the aperture averaging factor for different turbulence regimes have been investigated. It was shown that the stronger the turbulence, the steeper the initial decline with a higher saturation in the Aperture Averaging curves. The effect of aperture size at the receiver and the inner structure parameter in theory were also analyzed to monitor the change in the intensity variance as the Rytov variance increases. It has been seen that in theory using the scintillation index model for strong turbulence regimes ($\sigma_R > 1$), the inner structure parameter is commanding on the value of the intensity variance at small diameter values. Various Turbulence Strength estimation techniques as well as turbulence

frame acquisition methods are also developed to investigate the parameters that are involved in atmospheric optical turbulence in all turbulence regimes.

A practical method for creating turbulence like phase screens have been established in desired turbulence regimes. A new method for establishing the right measures of addition to the propagated beam has been constructed by arranging the influence of lower and faster fluctuations in each phase screens along the propagation. It has been found that faster fluctuations are more effective on the strong turbulent regimes whereas lower fluctuations are effective in weaker ones. Desired turbulence strength has been established with simulation by suggesting temporal fluctuations in the induced turbulence power in strong turbulence conditions. In order to see how realistic our simulation is, the AA and PAAA curves are also compared .

Bibliography

- [1] D. Kedar and S. Arnom, “Optical wireless communications through fog in the presence of pointing errors,” *Applied Optics*, vol. 42, no. 24, pp. 4946–4954, 2003.
- [2] L. C. Andrews, *Laser Beam Propagation Through Random Media*. Bellingham, Washington: SPIE Optical Engineering Press:, 1998.
- [3] L. C. Andrews, R. L. Phillips, and C. Y. Hopen, *Laser Beam Scintillation with Applications*. Bellingham, Washington: SPIE Press:, 2001.
- [4] L. C. Andrews, R. L. Phillips, and C. Y. Hopen, *Laser Beam Scintillation with Applications*. Bellingham, Washington: SPIE Optical Engineering Press, modern theories in the propagation of optical waves in a turbulent medium. p. 45-104 ed., 2001.
- [5] D. L. Fried, “Aperture averaging of scintillation,” *J. Opt. Soc. Am.*, vol. 57, pp. 169–175, 1967.
- [6] V. Tatarskii and trans. by R.A. Silverman, *Wave Propagation in a Turbulent Medium*. New York: McGraw-Hill, 1961.
- [7] S.Zamet and Y. Yitzhaky, “Turbulence strength estimation from an arbitrary set of atmospherically degraded images,” *J. Opt. Soc. Am., A*, vol. 23, December 2006.

- [8] J. Barron, D. Fleet, and S. Beauchemin., “Performance of optical flow techniques.,” *International Journal of Computer Vision*.
- [9] Z. S. Wu, H. Y. Wei, R. K. Yang, and L. X. Gou., “Study on scintillation considering inner and outer scales for laser beam propagation on the slant path through the atmospheric turbulence,” *Progress In Electromagnetics Research*, vol. 80, pp. 277–293, 2008.
- [10] H. Yuksel and H. Meric, “Simulation of beam propagation through turbulent media for diverse turbulence regimes,” *Laser Communication and Propagation through the Atmosphere and Oceans*, vol. 8517-16, August 2012.
- [11] J. D. Schmidt, *Numerical Simulation of Optical Wave Propagation with examples in Matlab*. Bellingham, Washington: SPIE Press, 2010.
- [12] J. M. Martin and S. M. Flatte, “Simulation of point-source scintillation through three-dimensional random media,” *J. Opt. Soc. Am. A*, vol. 7(5), pp. 838–847, 1990.
- [13] S. M. Flatte, G. Y. Wang, and J. Martin, “Irradiance variance of optical waves through atmospheric turbulence by numerical simulation and comparison with experiment,” *J. Opt. Soc. Am. A*, vol. 10(11), pp. 2363–2370, 1993.
- [14] L. Sjoqvist, M. Henriksson, and O. Steinvall, “Simulation of laser beam propagation over land and sea using phase screens- a comparison with experimental data,” *Proc. Of SPIE*, vol. 5989, no. 59890D, 2005.
- [15] J. Martin and S. M. Flatte, “Intensity images and statistics from numerical simulation of wave propagation in 3-d random media,” *APPLIED OPTICS*, no. 2711, pp. 2111–2125, 1998.
- [16] L. C. Andrews, “Aperture averaging of optical scintillations: power fluctuations and temporal spectrum.,” *Waves in Random Media*, vol. 10, 2000.

- [17] O. Tuzel, F. Porikli, and P. Meer, “Region covariance: a fast descriptor for detection and classification,” *European Conference on Computer Vision (ECCV)*, vol. Gratz, 2006 (oral).
- [18] I. W. Selesnick, R. G. Baraniuk, and N. G. Kingsbury, “The dual-tree complex wavelet transform,” *IEEE Signal Processing Magazine*, vol. 22, no. 6, pp. 123–151, 2005.
- [19] P. Reddy and D. Prasad, “Multiwavelet based texture features for content based image retrieval,” *IJCST*, vol. vol. 2 Issue 1, March 2011.
- [20] S. R. Gunn, “Support vector machines for classification and regression,” *ISIS Tecnical Report*, vol. University of Southampton, 1998.
- [21] H. Yuksel and H. Meric, “Study of strong turbulence effects for optical wireless links,” *Laser Communication and Propagation through the Atmosphere and Oceans*, vol. 8517-17, August 2012.
- [22] H. Yuksel, *Studies of the effects of atmospheric turbulence on free space optical communications, PhD Thesis*. Collage Park, MD: UMD Library, 2005.
- [23] M. F. Stell, C. I. Moore, H. R. Burris, M. R. Suite, M. J. Wilcheck, M. A. Davis, R. Mahon, E. Oh, W. S. Rabinovich, G. C. Gilberth, W. J. Scharpf, and A. E. Reed, “Passive optical monitor for atmospheric turbulence and windspeed,” *Free-Space Laser Communication and Active Laser Illumination III, Proc. of SPIE*, vol. 5160.
- [24] L. Andrews, R. Philips, C. Hopen, and M. Al-Habash, “Theory of optical scintillation,” *J. Opt. Soc. Am.*, vol. 16, no. 6, 1999.
- [25] J. Dunphy and J. Kerr, “Scintillation measurements for large integrated-path turbulence,” *J. Opt. Soc. Am.*, vol. 63, no. 8, 1973.

- [26] D. L. Fried, “Optical resolution through a randomly inhomogeneous medium for very long and very short exposures,” *J. Opt. Soc. Am.*, vol. 56, October 1996.
- [27] J. W. Strohbehn, *Laser Beam Propagation in the Atmosphere*. Verlag, Berlin: Springer, modern theories in the propagation of optical waves in a turbulent medium. p. 45-104 ed., 1978.
- [28] C. C. Davis and I. I. Smolyaninov, “The effect of atmospheric turbulence on bit-error-rate in an on-off-keyed optical wireless system,” *Free-Space Laser Communication and Laser Imaging, Proc. SPIE.*, vol. 4489, pp. 126–137, October 2002.
- [29] J. H. Churnside, “Aperture averaging of optical scintillations in the turbulent atmosphere,” *Appl. Optics*, vol. 30, pp. 1982–94, May 1991.
- [30] L. C. Andrews, R. L. Phillips, and C. Y. Hopen, “Aperture averaging of optical scintillations: power fluctuations and the temporal spectrum,” *Wave Random Media*, vol. 10, no. 2000, pp. 53–70.
- [31] L. M. Wasiczko, *Techniques to Mitigate the Effects of Atmospheric Turbulence on Free Space Optical Communication Links*. University of Maryland, ph.d. thesis ed., 2004.
- [32] L. J. Andrews, *Field Guide to Atmospheric Optics*. Bellington, Washington: SPIE, Field Guides, fg02 ed., 2004.
- [33] H. T. Yura and W. G. McKinley, “Optical scintillation statistics for ir ground-to-space laser communication systems,” *Appl. Opt.*, vol. 22, pp. 3353–3358, 1983.